Magnetic Fluids Based Heat Dissipators

Ricardo Moura Costa Pinto
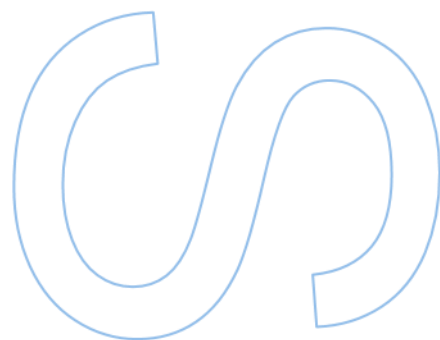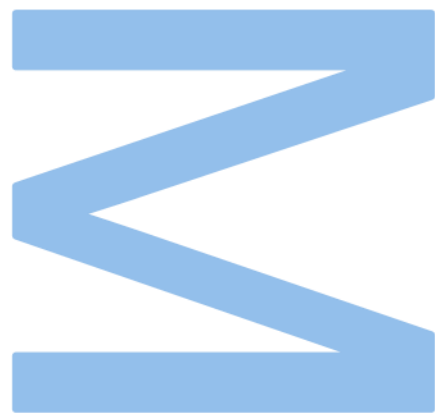M.Sc. in Physics Engineering
Department of Physics and Astronomy
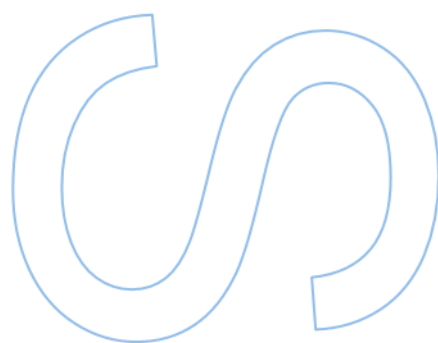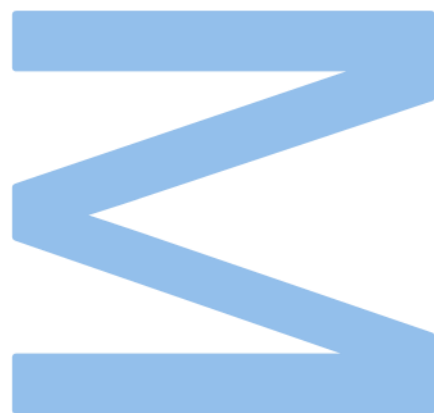2023

Supervisor
Dr. João Horta Belo,
Department of Physics and Astronomy
Faculty of Sciences of University of Porto

Co-supervisor
Dr. Ana Lúcia Pires
Department of Physics and Astronomy
Faculty of Sciences of University of Porto

" If plan A doesn't work, the alphabet has 25 more letters - 204 if you're in Japan. "

Claire Cook, Seven Year Switch

Acknowledgements

I would also like to thank my friends who have had a huge impact throughout my academic years, making it an experience I will never forget. Whether it was at parties (some of which I may have partially forgotten), at dinners, over a cup of coffee with a good conversation or even at the late night study sessions, these are all experiences that I will always cherish.

Finally, I would like to thank my family, who have undoubtedly been the most essential part of my being here at this moment, having been a constant source of motivation and support throughout my life. Honestly, words can not possibly do justice to how grateful I am, so I will simply end with a strong obrigado.

UNIVERSIDADE DO PORTO

Abstract

Faculdade de Ciências da Universidade do Porto

Departamento de Física e Astronomia

MSc. Engineering Physics

Magnetic Fluids Based Heat Dissipators

by Ricardo Moura Costa PINTO

Power electronics play an importante role in advancing technology. However, the pursuit of higher power densities have resulted in ever-increasing heat flows whose efficient dissipation and management is essential for the reliability and performance of any component. Conventional cooling methods such as air and water cooling exhibit limitations when it comes to handling high heat flows and consequently, liquid metals have gained an increasing attention due to their superior thermophysical properties.

This thesis consists of four section: i) Fabrication of galinstan, the MCM alloy and the mixtures of galinstan and MCM particles; ii) Thermomagnetic convection prototype testing; iii) COMSOL simulations of an MHD induction pump; iv) Testing of two MHD pumping prototypes, inductive and conductive.

In the first, magnetocaloric fluids with 2 wt%, 4 wt% and 6 wt% particle loadings mixed in galinstan, a liquid metal alloy at room temperature were fabricated and characterized. Both the manufactured mixtures and their individual components morphological, chemical, thermophysical and magnetic properties were characterized. A magnetic transition was observed at T = 33.5 ℃ for the mixtures, which is in agreement with what was expected for the Gd-Si-Ge alloy magnetic transition temperature, allowing us to conclude that galinstan does not alter the magnetic properties of the particles.

Subsequently, the mixtures were used in a heat dissipator prototype based on thermomagnetic convection with a thermal gradient of 7 ℃.

In addition to explore the propulsion of liquid metal by means of thermomagnetic convection, we also studied propulsion via magnetohydrodynamics. Our approach began by using COMSOL software to simulate the expected velocity profiles for a magnetohydrodynamic induction propulsion system as well as all the components required for its operation, such as the magnetic field, induced currents and Lorentz force.

Finally, we conducted tests on two prototypes: a magnetohydrodynamics induction pump based on the COMSOL simulations and a magnetohyrodynamics conduction pump. We observed a significant flow of galinstan in the magnetohydrodynamics conduction pump with a current of 5 A and a magnetic field intensity between 0.18 and 0.10 T.

In summary, in the first part of the thesis mixtures of galinstan with a Gd-Si-Ge alloy and its individual components were manufactured and characterized. These were then later tested in a prototype based on thermomagnetic convection. An induction MHD pumping system was also simulated in COMSOL, and the flow rate of the galinstan was studied as a function of the rotor frequency. Finally, two prototypes based on MHD pumping were tested: one by means of induction and the second via conduction. In the second one it was possible to observe a considerable flow of galinstan on the channel.

Resumo

Dissipadores de calor baseados em fluídos magnéticos

por Ricardo Moura Costa PINTO

A eletrónica de potência tem um papel importante no avanço da tecnologia. No entanto, com a procura de densidades de potência cada vez maiores surgem elevados fluxos de calor cuja gestão eficiente é essencial para a fiabilidade e o desempenho de qualquer componente. Os métodos de arrefecimento convencionais, como o arrefecimento a ar e a água, têm limitações quando se trata de lidar com elevados fluxos de calor. Por essa razão os metais líquidos têm ganho alguma popularidade devido às suas propriedades termofísicas superiores.

Esta tese consiste em quatro secções: i) Fabricação do galinstan, da liga do MCM e de três misturas de galinstan com partículas de MCM; ii) Testes de um protótipo de convecção termomagnética; iii) Simulações COMSOL de uma bomba MHD de indução; iv) Testes de dois protótipos de bombagem, um indutivo e o outro de condução.

Na primeira, fluidos magnetocalóricos com cargas de 2 wt%, 4 wt% e 6 wt% de partículas de MCM misturadas em galinstan, uma liga metálica líquida à temperatura ambiente foram fabricados e caracterizados. Tanto as propriedades das misturas fabricadas como dos seus componentes foram morfologicamente, quimicamente, termofisicamente e magneticamente caracterizadas. Uma transição magnética foi observada a T = 33.5 ºC nas misturas, o que está em linha com o esperado para a liga de Gd-Si-Ge fabricada, permitindo assim concluir que o galinstan não altera as propriedades magnéticas destas partículas.

As misturas foram posteriormente testadas num protótipo de um dissipador de calor baseado em convecção termomagnética sob a ação de um gradiente térmico de 7 ºC.

Para além de explorarmos a propulsão de metal líquido por convecção termomagnética, estudámos também a propulsão por magnetohidrodinâmica. Começámos por utilizar o

software COMSOL para simular os perfis de velocidade esperados para um sistema de propulsão por indução magnetohidrodinâmica, bem como todos os componentes necessários ao seu funcionamento, como o campo magnético, as correntes induzidas e a força de Lorentz.

Por fim, testamos dois protótipos, um de propulsão magnetohidrodinâmica por indução baseado nas simulações COMSOL e o outro propulsão magnetohidrodinâmica via condução. Tendo-se observado um fluxo considerável de galinstan para a bomba magnetohidrodinâmica de condução durante esta fase do estudo para uma corrente de 5 A e campo entre 0.18 e 0.10 T.

Em sumário, na primeira parte da tese, misturas de galinstan com partículas de uma liga de Gd-Si-Ge bem como os seus componentes individuais foram fabricados e caracterizados. Estes foram depois testados num protótipo baseado em convecção termo-magnética. Um sistema de bombagem MHD de indução foi simulado em COMSOL e tendo sido estudado o fluxo de galinstan em função da frequência do rotor. Por fim dois protótipos de bombagem MHD foram testados: um por indução e o segundo por condução. Tendo-se observado no segundo um fluxo considerável de galinstan no canal.

Contents

List of Figures

Chapter 1

Motivation

Power semiconductor devices are increasingly important in our society, with applications ranging from renewable energy systems to electric vehicles and industrial automation markets [1]. These devices handle high power densities and switching frequencies, enabling efficient power conversion and control. However, the increasing power requirements and miniaturization of electronic systems have led to higher heat fluxes generated by these devices [2], as can be seen in Figure 1.1a). High temperature is the main cause behind the malfunction or failure of electronics [3]. Figure 1.1b) shows the failure factor, which denotes the ratio of the failure rate at any given temperature to the failure rate at a fixed temperature of an electronic device as a function of temperature. It is evident from this figure that beyond 75 °C the failure rate of the device increases exponentially with temperature. For that reason, effective thermal management is essential to ensure their optimal performance, reliability, and longevity.
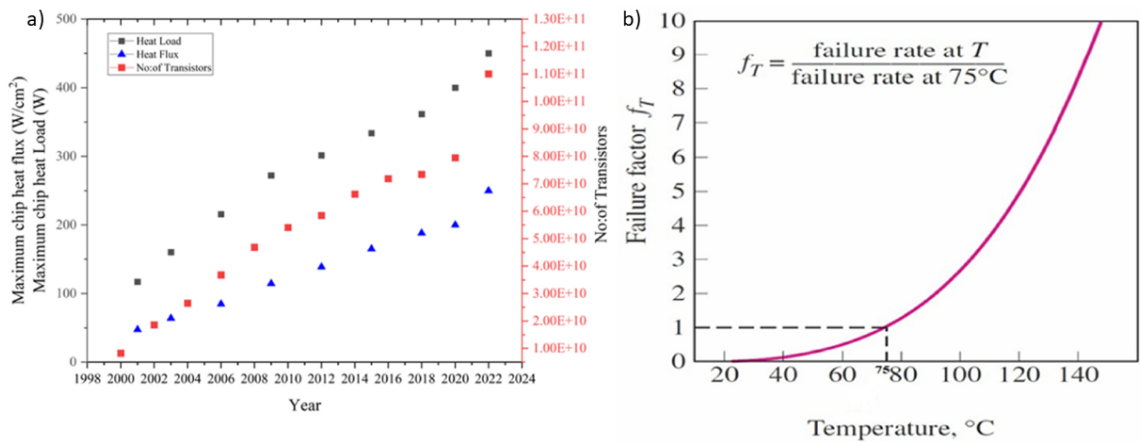
FIGURE 1.1: a) Number of transistors, heat flux and power consumption of microprocessor chips projections until 2022 b) Failure factor of a device as a function of temperature, image from [4].

Conventional cooling methods, such as air cooling, can only deal with small heat fluxes, typically below 100 W/cm^2 [5]. As can be seen in Figure 1.1a) air cooling solutions are nowhere near enough to handle even current chip heat fluxes. For that reason, there is a demand for new cooling alternatives capable of dissipating high heat fluxes (between 10^2 and 10^3 W/cm^2 [6]) at operational time speeds. Liquid mini and micro-channel cooling stands out as a technology capable of dealing with such heat fluxes, due to its favorable thermophysical properties including higher thermal conductivity compared to air [5]. Table 1.1 summarizes several thermophysical properties of different cooling fluids, such as $Ga_{68}In_{22}Sn_{10}$ (galinstan), water and Ethylene glycol. Galinstan has a high electrical conductivity, larger thermal conductivity when compared with water but lower heat capacity. It was shown by Hodes *et al.* [7] that in their optimized configurations a galinstan mini-channel should reduce the overall thermal resistance of the system by about 40% when compared to an optimized water micro-channel. One advantage of using room temperature liquid metals (RTLMs) as a cooling fluid is that due to their high electrical conductivity they can be wirelessly pumped, *i.e.* there is no need for mechanical pumps. This pumping mechanism relies on principles of magnetohydrodynamics (MHD) in which the coupling between magnetic field and current gives rise to a pumping Lorentz force [8].

Some recent studies have gone one step further and have created mixtures of RTLMs with magnetocaloric particles [9] [10]. This opens the possibility of pumping these mixtures through thermomagnetic convection, requiring only an applied magnetic field and a thermal gradient. In the case of heat dissipators, this thermal gradient is already inherent in the system, so the operation of this system would only need a magnetic field source, which would greatly reduce the electrical consumption of the heat dissipator.

TABLE 1.1: Thermophysical properties of various cooling liquids, adapted from [11]. * The physical properties of the fluid are based on a 60/40% ethylene glycol/water mixture.

Property	Unit	$Ga_{68}In_{22}Sn_{10}$	Water	Ethylene glycol*
Density	kg/m^3	6400	998	1107
Melting Point	$^\circ C$	11	0	-52.8
Specific Heat Capacity	$J/(kg \cdot ^\circ C)$	365	4081	3284
Dynamic Viscosity	$Pa \cdot s$	0.0024	0.001	0.009
Electrical Conductivity	S/m	$3.46 \cdot 10^6$	$5.5 \cdot 10^{-6}$	$3.2 \cdot 10^{-6}$
Thermal Conductivity	$W/(m \cdot ^\circ C)$	16.5	0.606	0.52

Chapter 2

Introduction and State of the Art

2.1 Liquid Metals

RTLMs are a distinct class of materials that possess the characteristics of both liquids and metals. Unlike conventional metals, which typically exist in a solid state at room temperature, RTLMs maintain a liquid form at ambient conditions. In nature there are only a limited number of elemental RTLMs or near room temperature liquid metals (NRTLMs) such as mercury (T_m = -39 ℃), francium (T_m = 21 ℃), gallium (T_m = 30 ℃) and cesium (T_m = 28 ℃), although issues such as radioactivity in francium and cesium limit their applicability. Due to the limited number of elemental RTLMs and NRTLMs, liquid metal alloys, such as gallium-based alloys and NaK, have become popular alternatives for various applications [12][13] [14]. These are used in a variety of applications, from liquid mirror telescopes [15], liquid metal photonics [16] to flexible electronics [17].

2.1.1 Mercury

Mercury (Hg) is perhaps the most well-known liquid metal. Due to its high thermal conductivity, it was historically used as the cooling fluid for the Clementine nuclear reactor [18]. However, the toxicity [19] associated with mercury as well as its relatively high vapor pressure that increases exponentially with temperature [20] limit its use nowadays. In fact, the European Union banned in 2017 several products containing mercury, such as thermometers, barometers and some electronic equipment [21].

2.1.2 Sodium Potassium Eutectic Alloy

NaK is an eutectic alloy, meaning it consists of a mixture of elements resulting in the lowest possible melting point of the mixture as shown in Figure 2.1. The eutectic composition for NaK occurs at approximately 77.5% potassium (K) and 22.5% sodium (Na), which gives a melting point of around -12.6 ℃ [22].
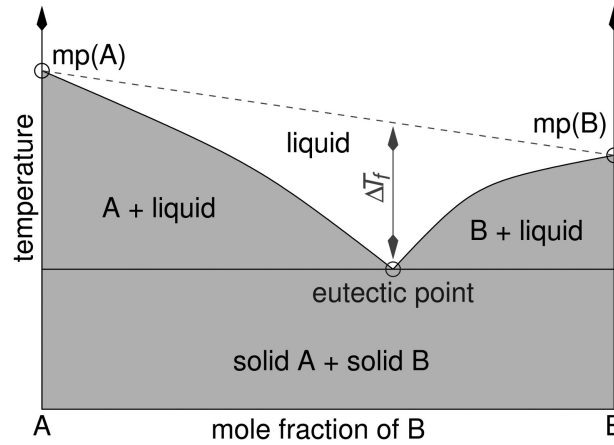
FIGURE 2.1: Representation of a eutectic point on a two-component phase diagram. image from [23]

Due to its relatively low vapor pressure, higher boiling point and lower toxicity, sodium potassium alloys as well as sodium alloys served as substitutes for mercury in several applications. In fact, this sodium alloys have been employed as coolants in nuclear power plants, in space applications such as satellites and more recently in CPUs [24] [25] [26]. While NaK has significant advantages as a RTLM coolant, its use presents some limitations associated with its high reactivity when in contact with water or humid air [27].

2.1.3 Gallium-based alloys

Gallium is an element with low toxicity and extremely low vapor pressure at room temperature [28]. Since gallium's melting temperature is slightly above room temperature (30 ℃) it is commonly alloyed with indium and tin to reduce its melting point (from 30 ℃ to 11 ℃ in the case of galinstan). The Ga-In-Sn phase diagram is represented in Figure 2.2.

Galinstan and Eutectic Gallium-Indium, $Ga_{75.5}In_{24.5}$, (EGaIn) are two of the most popular gallium based RTLM alloys with melting temperatures of 11℃ and 15.5℃, respectively [29]. These alloys have several advantageous characteristics such as high thermal conductivity, low viscosity, and relatively high electrical conductivity [30]. Galinstan for

example is used today as a substitute of mercury in thermometers [31] and as substitute for thermal paste, due to its higher thermal conductivity, for example in the Sony's Playstation 5 console [32]. For the past 20 years, gallium-based alloys have been studied as cooling fluids for the management of high heat flows. However, the use of liquid gallium-based alloys has some challenges, namely its price (upwards of 35 $/$ml$ with the used reagents), its corrosive nature towards some metals (alluminum, copper, among others [33]) and the development of a thin oxide layer on its surface when exposed to air, which may limit its applicability [34].
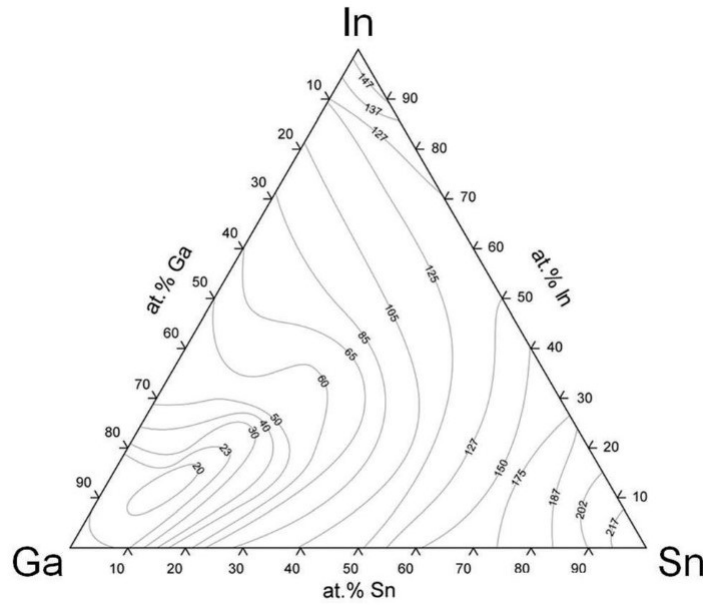
FIGURE 2.2: Ga-In-Sn phase diagram, image from [35].

To circumvent the corrosive nature of these alloys, coatings can be applied to the metals thus preventing direct contact with the fluid [36]. As for the surface oxide layer, this can be etched away using NaOH [37] or HCl [38]. Although the oxide layer is detrimental for some applications, it is essential for others. The oxide layer gives the fluid the ability to mechanically stabilize itself in non-equilibrium positions. Without the oxide layer the fluid, due to its high surface tension, would simply bead up [39]. This effect can be observed in Figure 2.3 in which the liquid metal is initially in a non-equilibrium state because of the oxide layer. Afterwards, the EGaIn is exposed to acid removing the oxide layer, resulting on the bead up of the metal. The existence of the oxide layer thus allows for applications in microfluidics [40], 3D printing [41] amongst many others.

Gallium-based alloys, particularly galinstan due to its low melting point, is a more viable solution for near room temperature cooling applications than mercury and NaK,

which is toxic and highly reactive with air respectively.
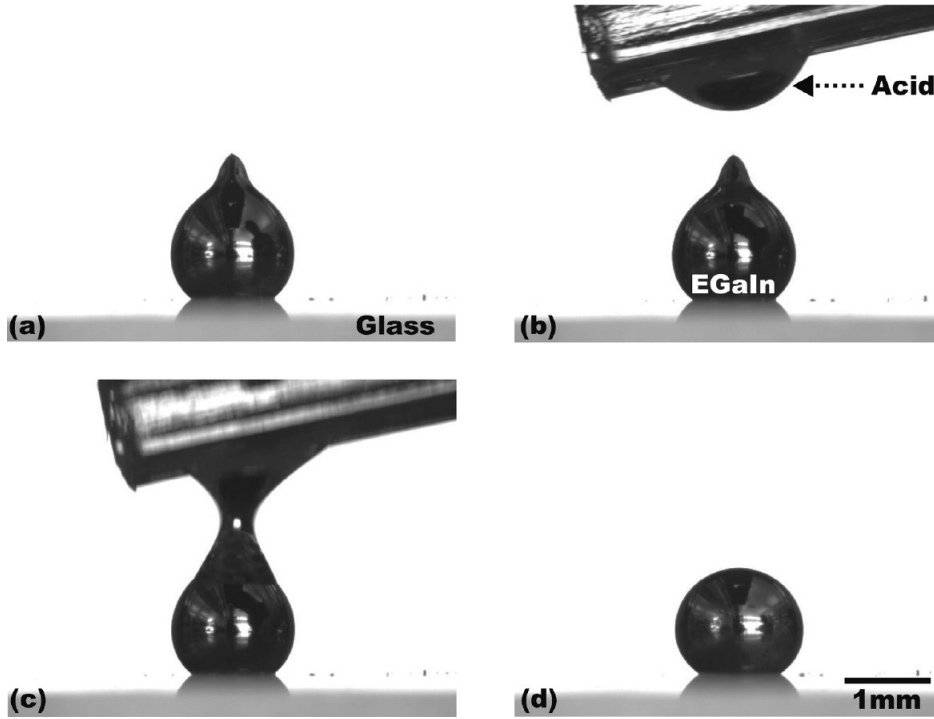
FIGURE 2.3: a) Liquid metal droplet in non-spherical shape due to the oxide layer; b-c) Removal of the oxide layer with acid (HCl); d) Liquid metal droplet beads up due to the high surface tension, image from [39].

In recent years, RTLMs have been mixed with magnetocaloric particles [9][10], thus allowing to control the fluid by the simple application of a magnetic field. This makes it an interesting fluid for various areas such as microfluidic applications [42], electronics [43] and refrigeration [9]. However, to the best of our knowledge, these mixtures of RTLMs with magnetocaloric particles have not yet been applied in thermomagnetic convection circuits. These circuit systems would allow the fluid to be pumped by only a magnetic field and a thermal gradient.

2.2   Magnetocaloric Effect

The magnetocaloric effect (MCE), first discovered in 1881 by E.Warburg [44], is an intrinsic property of all magnetic materials. The ordering of the magnetic moments of the material when subjected to a magnetic field will reduce the entropy associated to the magnetic moments sub-system. If this magnetization process is adiabatic and reversible, the total entropy of the system does not change hence, there has to be an increase of the entropy

of the lattice in order to compensate the entropy reduction from the magnetic moment system. Consequently, this leads to an increase in the materials temperature [45].

The MCE is usually quantified either by the isothermal entropy variation (ΔS_M), blue vertical line on Figure 2.4, or by the adiabatic temperature change (ΔT_{ad}), black horizontal line on that figure, under a magnetization or demagnetization process of a material.
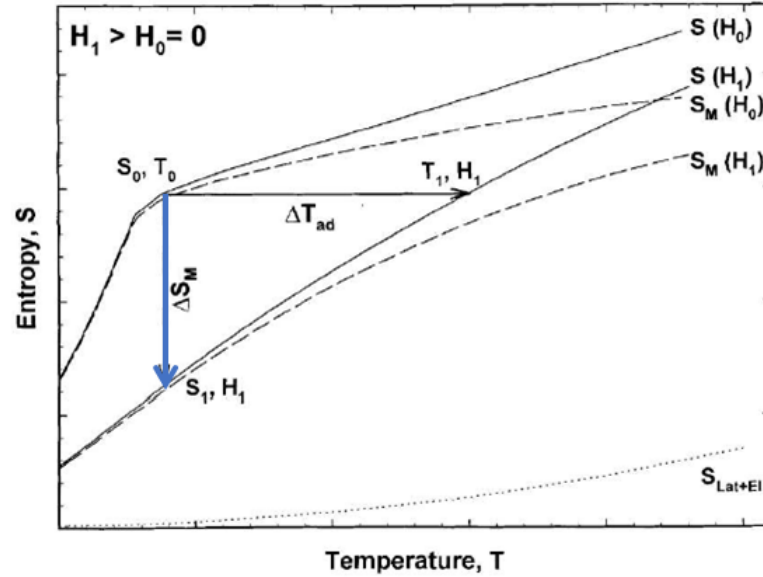
FIGURE 2.4: Entropy *vs* temperature plot in which the dotted line represents the combined lattice and electronic entropy, the dashed lines represent the magnetic sub-system entropy under different magnetic fields (H0 and H1) while the solid lines show the combination of both. The isothermal entropy change and the adiabatic temperature change are also illustrated by the blue vertical and black horizontal lines respectively, image adapted from [46].

The MCE serves as the foundation to construct thermodynamic cooling cycles, achieved through the magnetization and demagnetization of magnetocaloric materials and the heat exchanged with a carefully selected heat exchanger, Figure 2.5.
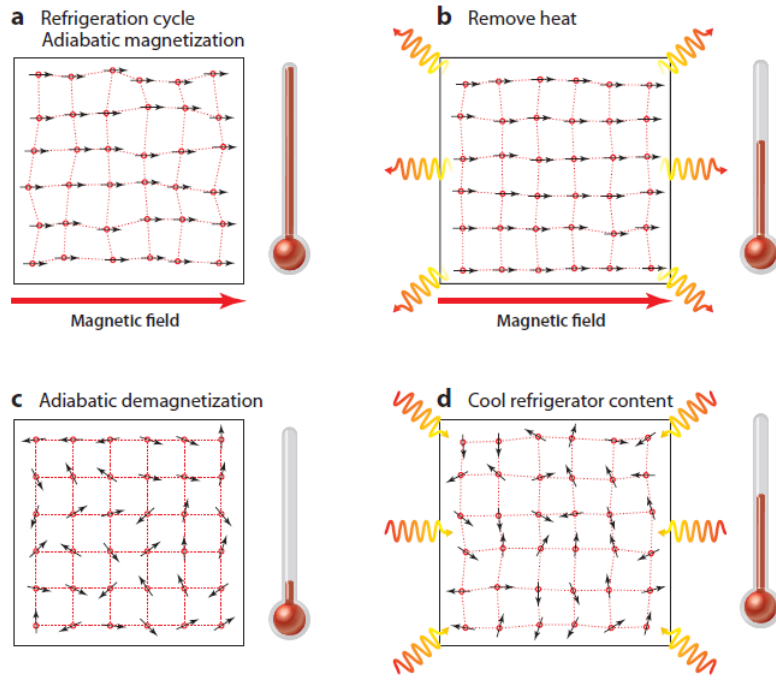
FIGURE 2.5: Schematic of a magnetic refrigeration cooling cycle. a) Adiabatic magnetization of the material resulting in an increase of its temperature; b) Removal of heat from the material via an heat exchanger while maintaining the applied magnetic field; c) Adiabatic demagnetization of the material resulting on the decrease of the material's temperature; d) Material absorbs heat from the surroundings thus increasing its temperature. Image from [47].

A magnetocaloric cooling process was first demonstrated in 1933 by Giauque and MacDougall, reaching temperatures as low as 250 mK through adiabatic demagnetization [48]. Presently, this technology finds applications in cryogenic temperatures, powering sub-kelvin cryostats, and is currently being explored for hydrogen liquefaction [49] [50]. It is also used in room temperature applications, boosted by the discovery of the giant magnetocaloric effect near room temperature in $Gd_5Si_2Ge_2$ by Pecharsky in 1997 [51]. Although there is still a long way to go for this technology to be competitive with current vapor compression cooling technologies it can already be found in the market on some specific applications such as beverage coolers [52] [53].

2.2.1 Measurement of the MCE

The MCE can be quantified through both direct and indirect measurement techniques [54]. Direct measurements of ΔT_{ad} consist on the direct measurement of the materials´s temperature change when subjected to a magnetic field intensity variation in adiabatic conditions. This type of measurement is not common in the scientific/engineering community as it can be quite challenging due to the requirement of adiabatic conditions and

good thermal contact between the sample and the thermal sensor [55]. Indirect measurements, on the other hand involve measuring the magnetization of the sample as a function of the magnetic field at different temperatures. Using Maxwell's relation from the equation (2.1) we can determine both the ΔS_M and ΔT_{ad} [56].

$$\left(\frac{\partial S}{\partial H}\right)_T = \left(\frac{\partial M}{\partial T}\right)_H \tag{2.1}$$

Rearranging the equation (2.1) and integrating under the magnetic field we obtain the following expression for the ΔS_M.

$$\Delta S(T) = \int_{H_i}^{H_f} \left(\frac{\partial M(H,T)}{\partial T}\right)_H dH \tag{2.2}$$

Then, we can determine in a similar fashion the expression for ΔT_{ad} having in mind that in a adiabatic process dS = 0.

$$\Delta T_{ad}(T) = \int_{H_i}^{H_f} \frac{T}{C_p(H,T)} \left(\frac{\partial M(H,T)}{\partial T}\right)_H dH \tag{2.3}$$

Comparing the equations (2.2) and (2.3) we can see that to determine the ΔS_M we only need to measure the magnetization as a function of the magnetic field for different temperatures, something relatively trivial to measure in any standard magnetometer equipment. As for the indirect measurement of ΔT_{ad} we need both the measurements of the heat capacity and magnetization of the material at different temperature and field values. It is worth highlighting from the above equations that the magnitude of the MCE is proportional to the derivative of the magnetization as a function of temperature, thus being maximized in temperatures near a magnetic phase transition [57].

Figure 2.6 shows the ΔS_M and ΔT_{ad} as function of temperature for $Gd_5Si_2Ge_2$ calculated using the equations above.
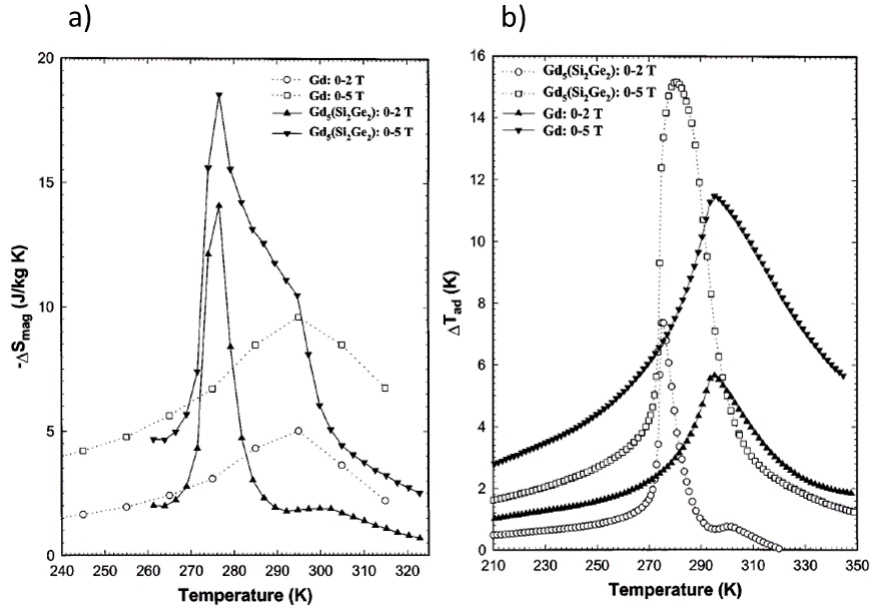
FIGURE 2.6: a) Entropy change of $Gd_5Si_2Ge_2$ as function of temperature from isothermal measurements for a magnetic field variation of 2 and 5 T respectively in comparison with the ΔS of Gd for the same values of magnetic field variation. b) Adiabatic temperature change as a function of temperature of $Gd_5Si_2Ge_2$ in comparison to Gd for magnetic field variations of 2 and 5 T. Image from [51].

2.3   Thermomagnetic Effect

The thermomagnetic effect consists in inducing phase transitions on a ferromagnetic material by supplying heat to a material when a magnetic field is being applied [58]. Considering a magnetized ferromagnetic material, by increasing its temperature, we will reduce its magnetization value because we are inducing a misalignment of the magnetic moments through thermal energy. If we now continue to increase the temperature, we will eventually reach the transition temperature, *i.e*, the Curie temperature (T_C), where the transition from a ferromagnetic state to a paramagnetic state takes place, thus resulting in a sudden drop in the magnetization. The magnetic materials can be divided into two large groups, those undergoing first-order (FOPT) and second-order (SOPT) phase transitions, being identified by analyzing their free energy derivatives and their depedence on temperature. In the case of materials presenting FOPT, the first derivative of the free energy (magnetization in this case) is discontinuous across the phase transition, while materials with SOPT show a discontinuity in the second derivative of the free energy (heat capacity) [59].

Similar to the MCE mentioned in the section above, the thermomagnetic effect is also larger when $\frac{\partial M}{\partial T}$ is larger, thus being maximized near the T_C of the material. As can be

seen in Figure 2.7, FOPT are much sharper than SOPT, hence presenting larger $\frac{\partial M}{\partial T}$, so materials with a FOPT generally present a larger thermomagnetic effect [60].
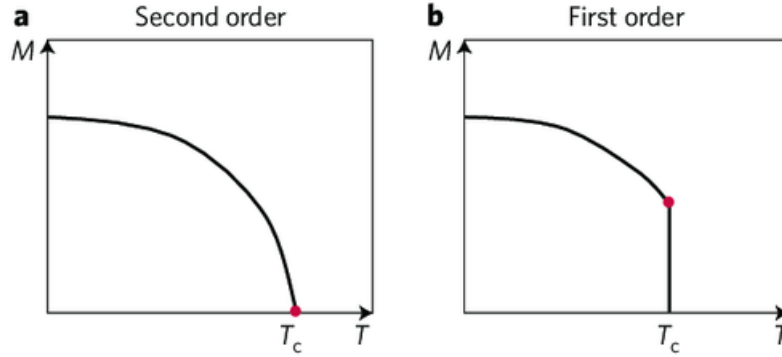
FIGURE 2.7: Magnetization vs temperature phase transition diagrams of a) second order phase transition and a b) first order transition marked by the discontinuity of the M(T) graph at T_C, adapted from [61].

However, unlike SOPT materials, they exhibit large hysteresis, which in the case of magnetic materials can be described as a mismatch between the magnetization response of the material to the application and removal of an external magnetic field. Which in turn results in a memory of their previous magnetic state even after the field is removed. This leads to energy losses over a magnetization-demagnetization cycle and is typically associated to the strong magnetovolume coupling exhibited by these materials. In fact, this strong magnetovolume coupling is also responsible for the general poor cyclability properties of these materials, as it typically leads to mechanical failure after several thermal/magnetic field cycles [62].

The thermomagnetic effect can be harnessed for several applications, such as motors, power generators [63] and self pumping of ferrofluids. Nikola Tesla proposed in 1889 the first thermomagnetic motor, as depicted in Figure 2.8.
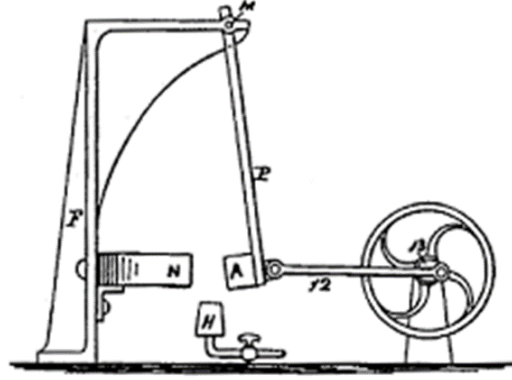
FIGURE 2.8: Diagram of Nikola Tesla's thermomagnetic motor, the armature A is attracted to the magnet's north pole N, being then heated by the gas burner H. When A transitions from a ferromagnetic state to a paramagnetic state it will be pushed away from the magnet because of the smaller magnetic susceptibility of material A at higher temperatures, that will then cool down to the ferromagnetic state being then again attracted to the magnet, thus resulting on the movement of the flywheel 13, image from [64].

Regarding the thermomagnetic generators, the working principle is similar to the thermomagnetic motor from Figure 2.8. Considering a ferromagnetic material in a magnetic circuit that uses a permanent magnet as a magnetic field source, changing its temperature will result in a change of the magnetization of the material. As a result of this temperature-induced variation in magnetization, the overall magnetic flux in the magnetic circuit changes[65]. This time variation of the magnetic flux now induces a voltage in a coil wound along the magnetic circuit as a result of Faraday's law of Induction [66]. Equation 2.4 represents the electromotive force ϵ induced in a coil with N turns by a time varying magnetic flux ($\frac{d\phi}{dt}$)

$$\epsilon = -N\frac{d\phi}{dt} \tag{2.4}$$

2.3.1 Thermomagnetic Convection

In recent years research has been done to harness the thermomagnetic effect to pump ferrofluids for cooling applications. Ferrofluids are colloidal suspensions of ferromagnetic or ferrimagnetic nanoparticles (typically below 10 nm [67]) within a carrier liquid such as water or kerosene [68]. The magnetic particles are coated with a surfactant to prevent agglomeration before being incorporated in the solvent.

An example of a thermomagnetic convection cooling circuit is shown in the Figure 2.9. Since the magnetic susceptibility of the ferrofluid, around T_C, is higher for lower temperatures, the cold ferrofluid will be more strongly attracted to the permanent magnet than the hot ferrofluid, thus generating a driving force actuating in the ferrofluid. The ferrofluid absorbs heat from the heat load, increasing its temperature and therefore reducing its magnetic susceptibility, being pumped away from the permanent magnet and towards the heat sink, where it will dissipate heat, cooling down and then returning to a state of high magnetic susceptibility. The pumping force is highly dependent on the concentration of nanoparticles in the ferrofluid and in the intensity of the applied magnetic field. Thus one can control the ferrofluid flow velocity by increasing the loading of nanoparticles or by substituting the permanent magnet with an electromagnet, making it possible to control the intensity of the magnetic field with the supply current and consequently control the fluid flow.
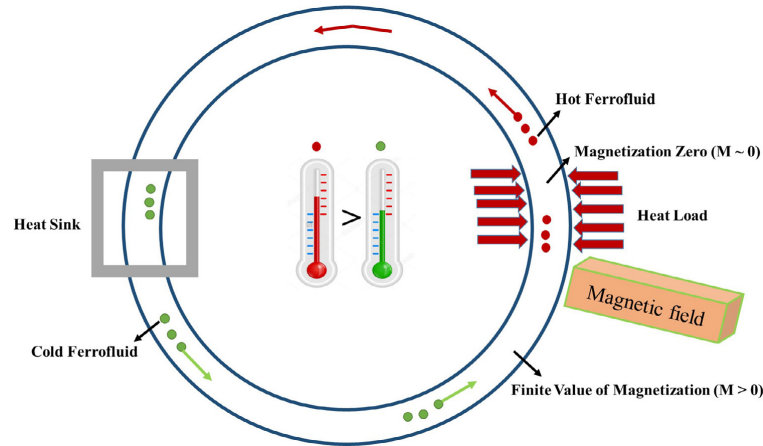
FIGURE 2.9: Schematic of a self-pumped ferrofluid via thermomagnetic convection, image from [69].

An interesting step forward now would be to combine the favorable thermophysical properties of RTLMs, such as high thermal conductivity, with a thermomagnetic pumping system with little to no electrical power consumption. Although there are many studies in the literature on thermomagnetic pumping and magnetic fluid metals, to the best of our knowledge there has not yet been any study harnessing the synergistic effect arising from combining these two.

In this thesis, we aim to fill in this scientific and engineering gap through the development of magnetic fluids by mixing galinstan and micro particles of $Gd_5Si_{2.4}Ge_{1.6}$, due to

its room temperature T_C, following the work of Filipa Furriel's thesis [70]. The production of the magnetic fluid and results are discussed in chapter 3 and 4 respectively.

COMSOL simulations were also carried out on a MHD induction pumping system, as well as testing two prototype MHD pumps, one via induction and the other via conduction, which are detailed and analyzed in chapters 3 and 4 respectively.

2.4   MHD Pumping

MHD is the field that studies the effects of the interaction between electrically conductive fluids and electric and magnetic fields [71]. Since the introduction of this topic to the present day, several MHD systems have emerged with applications ranging from submarine propulsion [72], energy harvesting [73] to liquid metal pumping [74] among many others.

MHD pumping of liquid metals working principle relies on the Lorentz force that arises from the combination of a current and a magnetic field, represented in equation 2.5.

$$\mathbf{F} = \mathbf{J} \times \mathbf{B} \tag{2.5}$$

Where F is the induced Lorentz force, J the current density, and B the magnetic flux density.

MHD pumps can be subdivided into two large groups, conduction pumps and induction pumps depending on the origin of the electrical current.

2.4.1   MHD Conduction Pumps

The operation of this type of pumps starts by applying an electric current through a conducting fluid orthogonal to an applied magnetic field. As a consequence of equation 2.5, the interaction of electric current and magnetic field generates a force that pumps the fluid in a direction orthogonal to both. Figure 2.10 ilustrates the induced Lorentz force upon the application of out-of-plane current and a in-plane magnetic field. There are two main types of MHD conduction pumps, DC and AC conduction pumps. In the first, we have a magnetic field perpendicular to an applied DC current. This type of pumps has been widely used for pumping liquid metal for cooling nuclear reactors [75]. However, in some fluids, the DC pumping can generate bubbles within the fluid (in the case of sea water, the current induces the water electrolysis thus forming bubbles of hydrogen and

oxygen), that not only reduces the pumping efficiency but also degrades the electrodes [76]. In the case of AC conduction pumps an AC current, synchronous with an AC magnetic field, is applied through the conducting fluid, and for high enough frequencies the reaction behind the production of the bubbles is reversed at high enough speed.

Some advantages of conduction MHD pumps are their simplicity and reliability due to lack of moving parts. Some challenges are the requirement of high currents, and electrode degradation from contact with the fluid.
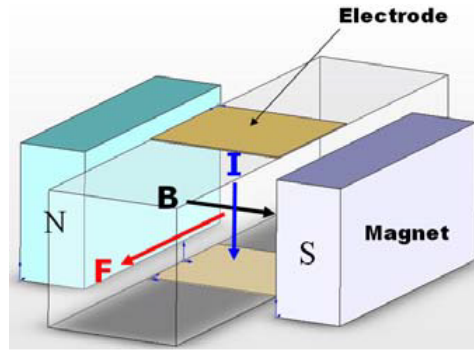
FIGURE 2.10: Schematic of a DC conduction MHDs pump, image from [77].

2.4.2 MHD Induction Pumps

MHD induction pumps, as the name suggests uses alternating magnetic fields to induce current in the fluid, as consequence of Lenz's law, a Lorentz force will then appear from the combination of the magnetic field and induced current. In comparison with MHD conduction pumps, these pumps present better stability, efficiency and performance [78]. There are two main groups of MHD induction pumps depending on the source of alternating magnetic field, that can be produced by: i) rotating permanent magnets (Figure 2.11); ii) electromagnets (or solenoidal coils).
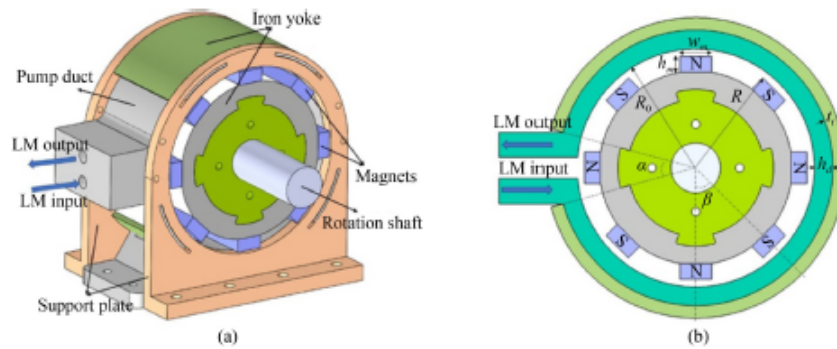
FIGURE 2.11: Schematic of a rotating permanent magnet MHD induction pump, image from [79].

A system with permanent magnets presents several advantages when compared to the use of coils, such as a less complex construction as well as a potentially higher efficiency since the Joule losses are negligible [80]. On the other hand, a coil system allows for the use of higher magnetic field frequencies which is essential to increase the magnitude of the induced currents. Based on this knowledge, in this thesis we set out to study an MHD induction pump based on rotating permanent magnets to pump galinstan into a mini-channel for application in a heat dissipator in addition to the thermomagnetic convection heat dissipator discussed on the section above.

Chapter 3

Experimental Methods

The work done in this thesis is divided into four main groups: i) Fabrication of galinstan, the magnetocaloric material (MCM) alloy and the mixtures of galinstan and MCM particles; ii) Thermomagnetic convection prototype testing; iii) COMSOL simulations of an MHD induction pump; iv) Testing of two MHD pumping prototypes, inductive and conductive.

3.1   Galinstan production

The galinstan used throughout this thesis was produced following the experimental procedure reported by Isabela A. de Castro, *et al.* [81]. We started by measuring the mass of a gallium ingot purchased from Fisher Scientific [82] with a purity of 99.99%. Given the stoichiometry of galinstan (68:22:10) we determined the corresponding masses of indium and tin to be weighed. The indium and tin ingots used were purchased from AlfaAeser [83] and thermoscientific [84] respectivily and both reagents had a purity of 99.99%. The reagents were weighted in a Kern® ABT 100-5M analytical balance.

The reagents were placed in a goblet immersed in a sand bath as can be seen in the Figure 3.1a). The temperature was set using a hot plate, and monitored with a thermometer that was in contact with the goblet. The temperature was slowly raised, and the reagents were thoroughly mixed throughout the melt with a glass stirring rod (a video of the galinstan preparation can be found here *). Despite the different melting points of the reactants (30 °C for Ga, 157 °C for In and 232 °C) the reagent mixture was already molten for a temperature of 100 °C. This can be explained by the liquid gallium dissolving the indium and

---

*https://drive.google.com/drive/folders/1UO7xhcNqNwQeVx5PNZDaRjcSfAHKOv3g?usp=sharing
Video of the galinstan production

tin [35]. Nevertheless, we continued to heat and mix our melt until a temperature of 150 ºC was reached.

It is important to note, that the temperature measured does not correspond to the actual temperature of our mixture, since it is in direct contact with the goblet, and therefore corresponds to an over-approximation of the actual temperature of the mixture.

Finally, we let the mixture cool down to room temperature, while maintaining its liquid state. Then the galinstan was transferred to a small glass container (Figure 3.1b)) using a plastic pipette. During the transfer we made sure to avoid the oxide layer formed in the surface of the galinstan.

a)

b)
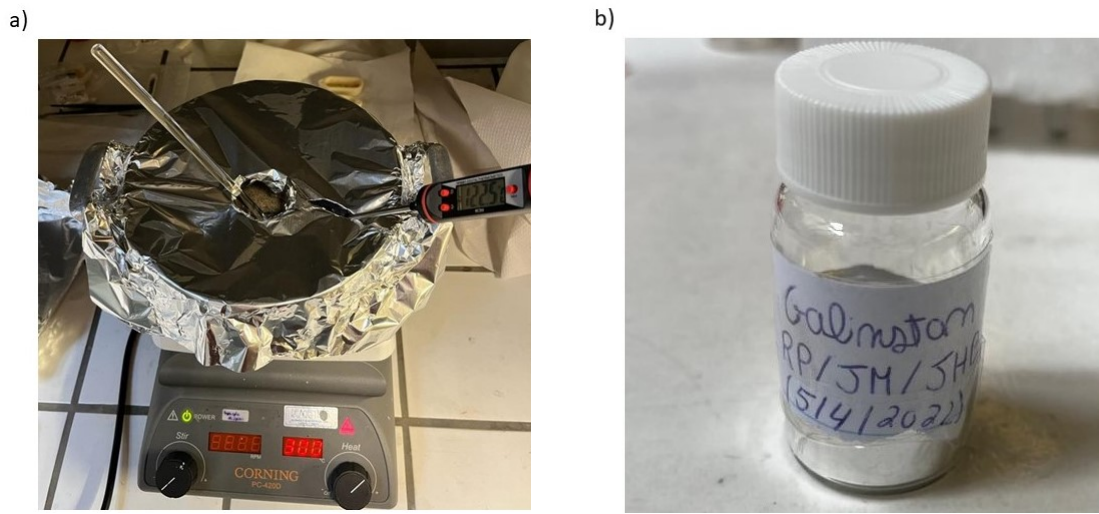
FIGURE 3.1: a) Ga-In-Sn melting setup, an aluminum pan filled with sand is heated by direct contact with an hot plate. A small goblet with the reagents is immersed in the sand while being constantly mixed and its temperature measured with a thermometer; b) Synthetized galinstan stored in a glass container.

3.2   Arc-Melting

The production of the $Gd_5Si_{2.4}Ge_{1.6}$ button began with the measurement of the reactants (Gd-Si-Ge) masses, according to the alloy´s stoichiometry, with an high-precision scale. The reagents were then placed into an arc-melting furnace. The lower melting point reagents were covered by higher melting point reagents to minimize potential evaporation losses. In order to minimize the oxidation of the alloy during the melting and solidification process, a vacuum of 10^{-5} mbar is established in the chamber, then the chamber is filled with high purity argon (around 800 mbar), an inert gas, as a purging process. This

purging is repeated three times before the first melt in order to strongly reduce oxygen content in the chamber.

For the first melt we began by opening the water-cooling circuit in order to prevent the melting of the copper base and the tungsten tip. Afterwards we place the tungsten tip close to the copper (without touching) and set a high enough voltage difference between them resulting in an electric arc. Subsequently, we begin to heat up the titanium getter since it absorbs gases, such as oxygen, when heated to temperatures above 700 ℃ [85]. Finally, with circular tip movements we begin to melt our sample, that due to surface tensions gains a spherical shape. In between consecutive melts both the getter and the button were flipped and the aforementioned protocol repeated until three melts were accomplished.

The arc-melting furnace used was an Edmund Bühler AM 500, capable of reaching temperatures of up to 3500 ℃. A schematic of the furnace can be seen in Figure 3.2.
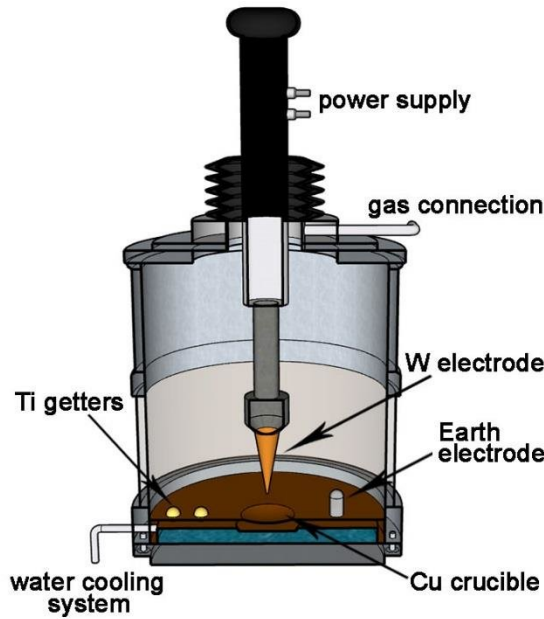
FIGURE 3.2: Schematic of an arc-melting furnace, image from [86].

3.3 Magnetic Fluid

The fabrication of the magnetic fluid began by defining the different loadings of $Gd_5Si_{2.4}Ge_{1.6}$ micro particles to be mixed in the produced galinstan. Three mixtures were fabricated with nominal loadings of 2 wt%, 4 wt% and 6 wt%. These loadings correspond to the mass percentages that we try to incorporate into our galinstan, which may differ from

the percentage successfully incorporated into the galinstan experimentally. The masses of magnetocaloric material were measured assuming a volume of 1 mL of galinstan. The incorporation of the $Gd_5Si_{2.4}Ge_{1.6}$ particles into the galinstan was done in a Aldrich® AtmosBag glove bag in order to minimize the oxidation of galinstan during the fabrication of the mixture. Figure 3.3 shows the used glove box as well as the required tools for this process.

After sealing the glove box, a purging protocol was repeated four times by alternatively establishing a low pressure (down to below 10 mbar with a vacuum pump) and filling the glove box with high purity argon (99.9999% pure). After that, an agate mortar and pestle were used to incorporate the magnetocaloric microparticles into the galinstan. Then, the mixture was grinded until a homogeneous appearance was achieved [†].

Afterwards the mixture is pipetted into an eppendorf and its magnetic properties are tested by approximating an array of NdFeB permanent magnets. Even though the mixture was fabricated in a glove box, it still developed a thin oxide layer in its surface. For that reason the pipetting of the mixture was made as described in section 4.1.

FIGURE 3.3: Experimental material used for the production of the magnetic fluid, a glove box, 1- Vacuum pump outlet; 2- Glass flask with the fabricated galinstan; 3- Eppendorfs with the measured masses of Gd-Si-Ge alloy powder; 4- Array of squared NdFeB permanent magnets; 5- Plastic pipette; 6- Agate pestle and mortar; 7- Inert gas inlet.

[†] https://drive.google.com/file/d/1Vem3PlUQjQHgyn8mtZrXEe1nP2JNYOCp/view?usp=sharing
Video of the fabrication of the magnetocaloric fluid

3.4   X-Ray Diffraction

When x-rays interact with the atoms within a crystal they undergo diffraction, resulting in constructive and destructive interference (Figure 3.4). This process yields a diffraction pattern, which carries valuable information about the crystal's atomic arrangement. Diffraction is possible with x-rays due to its low wavelength (λ), in the order of magnitude of the interatomic distances.
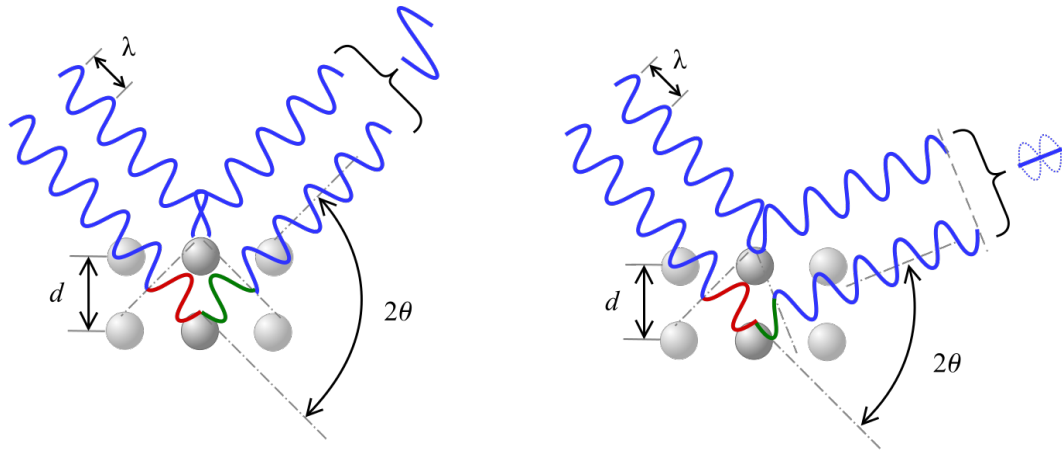
FIGURE 3.4: Schematic of Bragg´s X-Ray diffraction formulation; at the left constructive interference; at the right destructive interference, image from [87].

X-ray diffraction (XRD) can be explained by Bragg's law, formulated by Sir William Henry Bragg and his son Sir William Lawrence Bragg in 1913 [88]. Bragg's law describes diffraction according to equation 3.1.

$$n\lambda = 2dsin(\theta) \tag{3.1}$$

Constructive interference occurs when two times the spacing between crystal lattice planes (d) times the sine of the incidence angle (θ) is equal to an integer multiple (n) of the x-ray wavelength (λ). When this condition is met it results in a Bragg peak of the diffraction pattern. Since the wavelength of the x-rays will be constant throughout the measurements, the diffraction pattern will be obtained by probing x-ray intensity peaks as a function of the incident angle. The spacing between crystal lattice planes in a cubic ($a = b = c$), tetragonal ($a = b \neq c$) or orthorhombic ($a \neq b \neq c$) cells can be related with the lattice parameters a, b, c by equation 3.2.

$$\frac{1}{d_{hkl}^2} = \frac{h^2}{a^2} + \frac{k^2}{b^2} + \frac{l^2}{c^2} \tag{3.2}$$

Where h, k, l represents the Miller indexes, each peak corresponds to a given direction hkl [89].

The XRD measurements were performed in a Rigaku® SmartLab XRD with the Smart-Lab Guidance software. A 9 kW rotating anode with a copper target was used to produce the x-ray radiation. The radiation used was Cu K_α with $\lambda = 1.5418740$ $\mathring{A}$ as a nickel filter was used to filter out K_β radiation. A Bragg-Brentano configuration with a θ-2θ geometry was used, while 2θ was scanned from 10 º to 90 º with a step size of 0.01 º. With these measurements we were able to determine the percentages of crystalline phases present in our fabricated alloy through a LeBail refinement.

3.5   SQUID Magnetometry

A superconducting quantum interference device (SQUID) magnetometer is a type of induction magnetometer. The magnetic moment is indirectly measured by measuring the voltage change induced in a coil by a changing magnetic field of a moving magnetized sample.

The signals induced in the pick-up coils by changing the vertical position of the sample are then inductively coupled to the SQUID itself that measures voltage oscillations that are quantified in units of flux quantas. Through previous measurements of a standard callibrated sample, fit the voltage vs displacement curve, enabling the determination of the magnetic moment.Then by dividing the total magnetic moment by the sample mass or volume we are able to determine the magnetization.

The SQUID equipment used throughout this thesis was a Magnetic Properties Measurement System 3 (MPMS3) from Quantum Design [90]. Its superconducting magnet can generate magnetic fields up to 7 T. The temperature can also be controlled from 400 K down to 1.8 K. The pick-up-coil geometry of the system is constituted by four superconducting coils (Figure 3.5). The two pairs of coils are set in a opposed series configuration which removes contributions from external magnetic fields, such as the applied magnetic field [91].
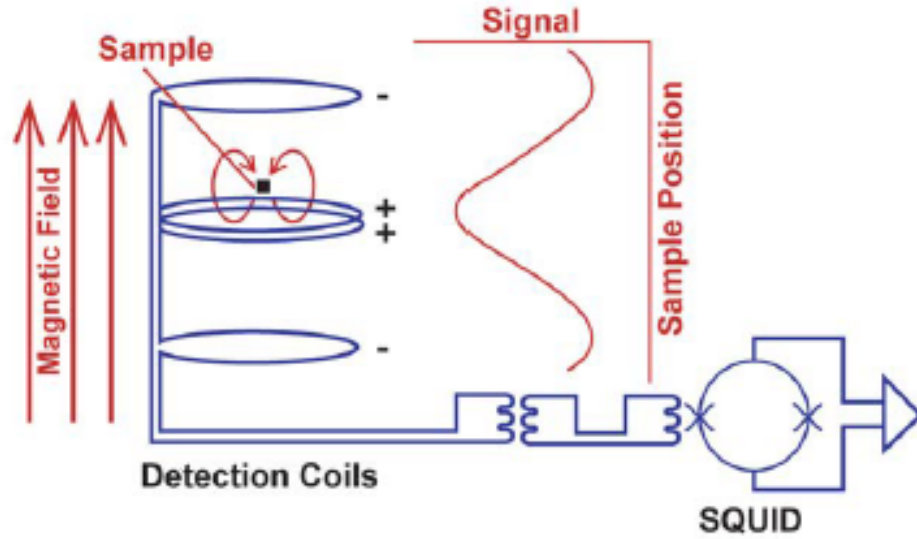
FIGURE 3.5: Pick-up-coil geometry of a SQUID magnetometer, image from [90].

The SQUID was used during this work for two main purposes: to study the magnetic transition of the fabricated MCM powder and its MCE, and to study the mixtures of galinstan with the MCM particles. For the powder, it is possible to estimate the T_C of the material using isofield magnetization as a function of temperature (M(T)) curves and to quantify the magnetocaloric effect indirectly by measuring isothermal magnetization as a function of magnetic field (M(H)) curves at temperatures around T_C and using the equation 2.2 to determine ΔS. With regard to mixtures, SQUID measurements make it possible to quantify the loading of mixed particles in the galinstan by comparing the M(H) curves of the mixture with the M(H) curves of the MCM powder. Measurements of the magnetic moment of fluids take extra care compared to powders. For example, it would not be possible to obtain a viable measurement using VSM, since on we would spread the sample across the sample holder, thus invalidating the initial centering process of the sample, which is one of the assumptions of these measurements. On the other hand, as the fluid is conductive, if we used VSM we would be inducing currents in the sample which would result in artifacts in the measurements.

3.6   SEM-EDS

The resolution limit achievable in a microscopy system is dependent on the wavelength of the "illumination" source used. In conventional optical microscopes this illumination

is done using light that in turn has a high wavelength, which limits the resolution achievable, around 200 nm, at best [92]. In scanning electron microscopy (SEM), since we are using an electron beam, we can achieve better resolutions (1 to 20 nm) due to the reduced and controllable electron beam wavelength.

The operation of the SEM begins by producing a beam of electrons which in turn is accelerated by an electron gun, this beam is then focused and directed to the sites of interest by a set of condenser lenses, scanning coils and objective lenses [93]. This beam is directed within a chamber where the specimen under study is located, it is important to note that both the chamber, the electron gun and all the path traveled by the electron beam are under a high vacuum so that there is little particle intereference/scattering in the focusing and scanning process with the electron beam [94].

The interaction between the electron beam and the sample produces a variety of signals, as can be seen in Figure 3.6, where secondary electrons, backscattered electrons and characteristic x-rays stand out, which are acquired from a set of specific detectors positioned in the SEM sample chamber and then analyzed by the imaging software.
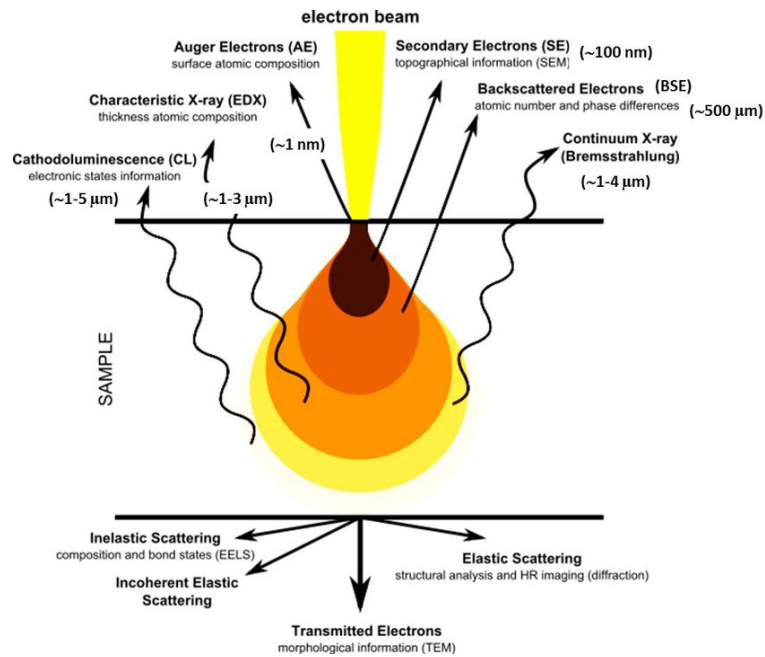
FIGURE 3.6: Various signals resulting from the interaction between an electron beam and the sample, image from [95].

Each of these signals provides different information ranging from the topography of the sample surface to its chemical composition. When the electron beam hits our sample, secondary electrons are produced from the emission of electrons from the valence layers of the constituent atoms of the sample. Since these electrons have a low energy ($E <$

50 eV) only those coming from layers close to the material´s surface are detected, thus containing information about the topography of the sample surface [96].

Backscattered electrons are more energetic electrons than secondary electrons and are generated by elastic scattering of electrons from the main electron beam. The coefficient of backscattered electrons created per number of total electrons strongly depends on the atomic number of the sample, a higher atomic number results in a higher coefficient and consequently a higher number of backscattered electrons. In this way these electrons can be used to create images where the contrast is given by differences in atomic number in the sample.

Characteristic x-rays are formed when electrons from an outermost layer decay to free inner layers due to collisions with electrons from the beam. The energy of these emitted x-rays is specific to each element, so it can be used to perform an elemental analysis of the sample. These x-rays are detected and analyzed in the form of an intensity versus energy spectrogram. This technique is called Energy-dispersive X-ray spectroscopy (EDS).

3.7   Differential Scanning Calorimetry

Differential Scanning Calorimetry (DSC) is a technique used to quantify the heat absorbed or released by a material when its temperature is being controlled [97]. The DSC measures the difference between the heat flow rate of a reference and the sample. The heat flow is calculated by equation 3.3 where $\frac{dQ}{dt}$ is the heat flow, T_s the sample temperature, T_r the temperature of the reference and R the thermal resistance from the heat source to the sample that is approximately equal to the thermal resistance from the source to the reference.

$$\frac{dQ}{dt} = \frac{T_s - T_r}{R} \tag{3.3}$$

For the DSC measurements we defined two measurement protocols, one for $Gd_5Si_{2.4}Ge_{1.6}$ powder and the other for samples produced with galinstan. The first protocol began by measuring the MCM powder mass in an aluminum pan. The pan was loaded into the DSC and its temperature was lowered down to -100 ºC, afterwards the temperature was cycled between -100 and 100 ºC with a rate of 10 ºC/minute while recording the heat flow as a function of temperature in a thermogram.

The samples with galinstan had to be measured with alumina pans since galinstan corrodes aluminum [98]. Since we changed the sample holder, a recalibration of the machine

was required. We started by measuring a new baseline with an empty alumina sample holder. The new calibration was then validated by measuring the melting and solidification of a certified indium standard. Afterwards, we measured the galinstan samples mass and loaded them in the DSC and after cooling it down to -100 ℃ the temperature was cycled between -100 and 100 ℃ at a rate of 10 ℃/minute.

From a thermogram, such as the one in Figure 3.7, one can identify if an event is endothermic or exothermic (melting and crystallisation peaks in Figure 3.7 respectively), as well as the temperature at which it takes place and the amount of heat involved.

All the DSC measurements were made with a TA Instruments® DSC25 calorimeter at the Institute for Energy Technology (IFE), in Norway. With these measurements we were able to determine the melting and solidification temperatures of our fluid, as well as analyze the magnetic transition of our MCM.
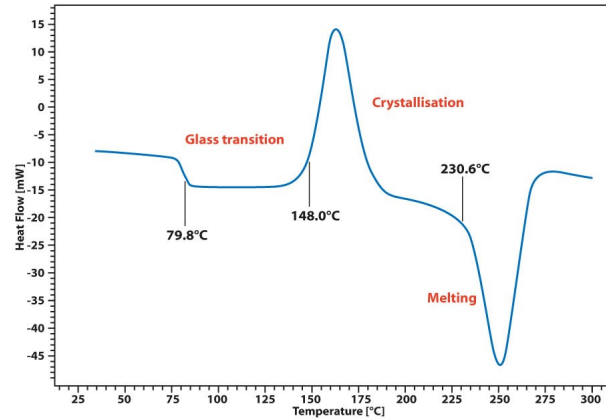
FIGURE 3.7: Example of a DSC thermogram, image from [99].

3.8 COMSOL MHD induction pump

A finite element method (FEM) model was developed to simulate an MHD induction pump in the COMSOL Multiphysics software. We started by creating the geometry of our pump, as illustrated in Figure 3.8. It is made of a rotor with 12 embedded permanent magnets with dimensions 5x3mm and a mini-channel with a diameter of four millimeters. The rotors velocity is modeled by setting a rotating domain from a moving mesh. Afterwards we assigned materials to the various components, such as, galinstan to the mini-channel, NdFeB to the permanent magnets and for simplicity air to the remainder of the geometry.

To simulate the problem, we imported three physics interfaces from COMSOL, the magnetic fields (mf), the laminar flow (spf) and the magnetohydrodynamics (mhd).
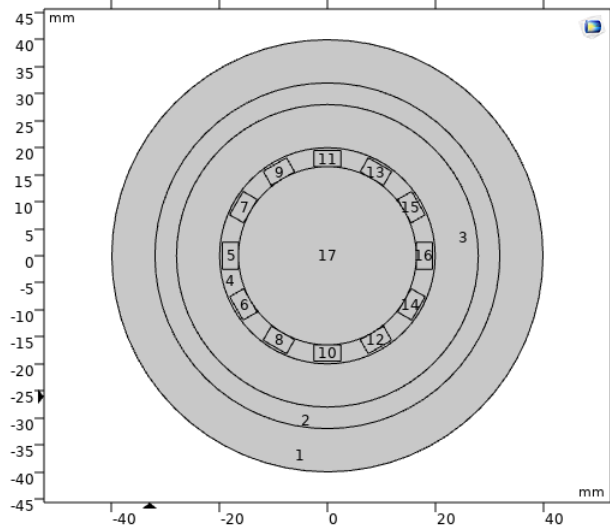
FIGURE 3.8: Geometry design of the MHD induction pump on COMSOL: 2) galinstan channel; 5-16) NdFeB permanent magnets. The remaining geometry is composed of air.

Magnetic Fields (mf)

The magnetic fields interface starts by setting a magnetic insulation in the outer boundary of our geometry and solves the Maxwell equations for the entire geometry by setting an "Ampère's Law" interface. Afterwards with the "magnets" embedded interface, we define our permanent magnets by setting their magnetic properties according to the corresponding material and define the magnetic poles. In our setup the permanent magnets are alternatively magnetized.

Laminar Flow (spf)

The galinstan flow is modelled in the Laminar Flow interface by solving both the Navier-Stokes and the continuity equation for incompressible fluids. As for the boundary conditions we manually selected the walls of the channel and defined a no slip condition.

Magnetohydrodynamics (mhd)

Finally, to couple both the fluid flow, the magnetic fields, and the induced currents we used the magnetohydrodynamics interface. A Lorentz force was introduced by coupling the alternating magnetic field of the rotating permanent magnets with the induced currents generated via Lenz's law by equation 3.4.

$$\mathbf{F} = \mathbf{J} \times \mathbf{B} \tag{3.4}$$

The interface also solves Ohm's law for the current density J of a conducting fluid moving with a velocity u in a magnetic field B (equation 3.5).

$$\mathbf{J} = \sigma(\mathbf{E} + \mathbf{u} \times \mathbf{B}) \tag{3.5}$$

3.8.1 Meshing and Studies

After defining the physics of the problem, we applied a mesh to the entire geometry. Additionally, two studies were performed, firstly a stationary study in which both the magnetic fields and fluid flow equations are solved. Since there is no movement, we are only solving for an initial stationary magnetic field thus we are not inducing current in the galinstan. Afterwards we performed a time dependent study, while setting the results of the stationary study as initial conditions.

The time dependet study allows the analysis of the temporal evolution of the magnetic field, as well as for the induced current densities in the fluid. We were also able to study the velocity of the fluid inside the mini-channel and the induced Lorentz forces.

3.9 Thermomagnetic cooling circuit prototype

In order to study the thermomagnetic convection of the produced magnetic fluids we built the setup pictured in Figure 3.9. It consists of an acrylic mini-channel with 4mm of diameter. The channel is filled with the magnetic fluid and a temperature gradient is imposed using a TEC1-12706 Peltier. The thermal contact between the fluid and the Peltier was achieved with copper tape. Finally, an array of 6 Nd-Fe-B permanent magnets with 20 x 20 x 2 mm dimensions, was set near the heat load part of the circuit, as portrayed in Figure 2.9. The magnetic field intensity was also studied as a function of distance as represented on Figure 3.10. As we can see the magnetic field intensity varies between 0.18 (at 5mm from the surface) and 0.10T (at 9mm from the surface) on the channel.
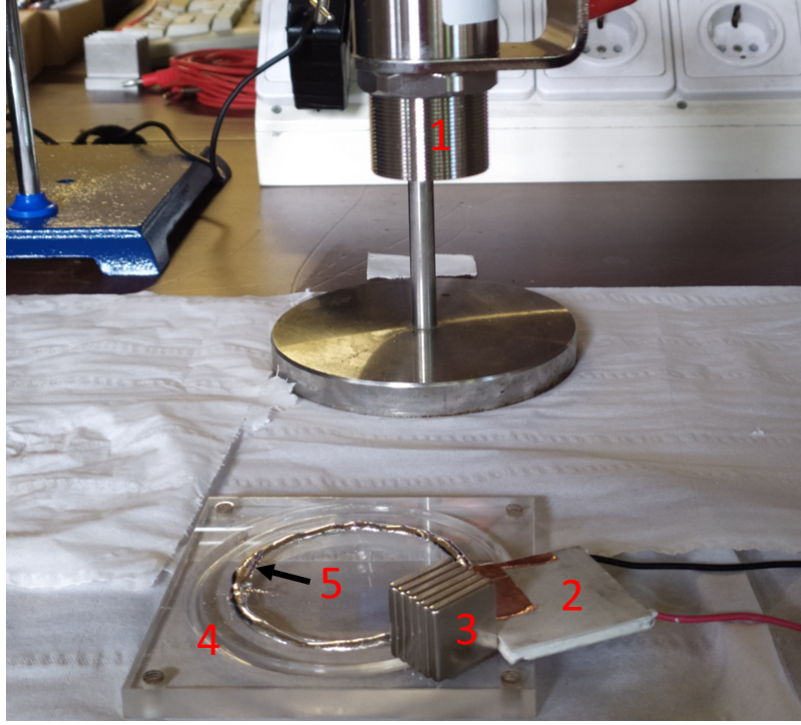
FIGURE 3.9: Experimental setup of the thermomagnetic cooling circuit; 1- Thermal camera; 2- Peltier with copper tape; 3- Array of squared NdFeB permanent magnets; 4- Acrylic mini-channel; 5- Produced magnetic fluid.
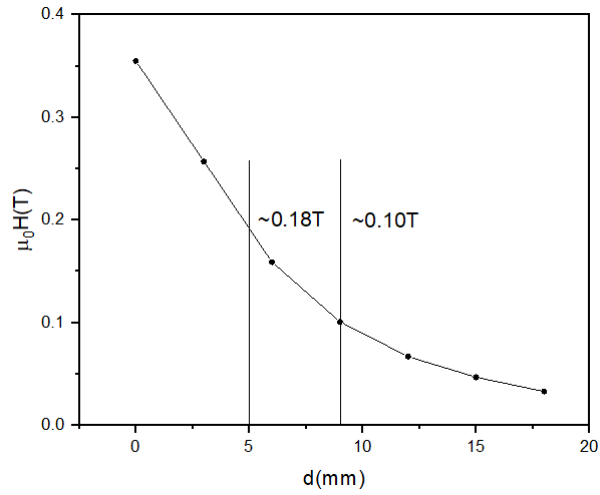
FIGURE 3.10: Magnetic field intensity of the permanent magnet array as a function of distance measured with a Gauss meter, the vertical lines represent the magnetic field in the boundaries of both walls of the magnetic fluid chanel.

The thermal camera used is an Optris Xi 400, which takes its measurements using infrared (IR) radiation. As the fluids used are metallic (and hence highly reflective), it is difficult to see small flow rates with the naked eye, making it essential to use a thermal camera to identify them.

3.10 Magnetohydrodynamics cooling circuit prototype

Two home-made prototypes based on MHD pumping were tested. The first one is a follow-up to the COMSOL simulation, based on induction of currents in the galinstan using an alternating magnetic field. While the second one relies on the coupling between a static magnetic field perpendicular to an applied DC current.

3.10.1 MHD induction pump

The MHD induction pump prototype is made of a rotor with 12 permanent magnets moved by a DC motor, and a 3D printed PLA channel with 4mm of diameter as can be seen in Figure 3.11. The rotor is set in plane with the channel thus a in plane rotation generates out of plane current loops within the galinstan. The coupling between the current loops and radial magnetic field will then generate a tangential Lorentz force in the fluid.
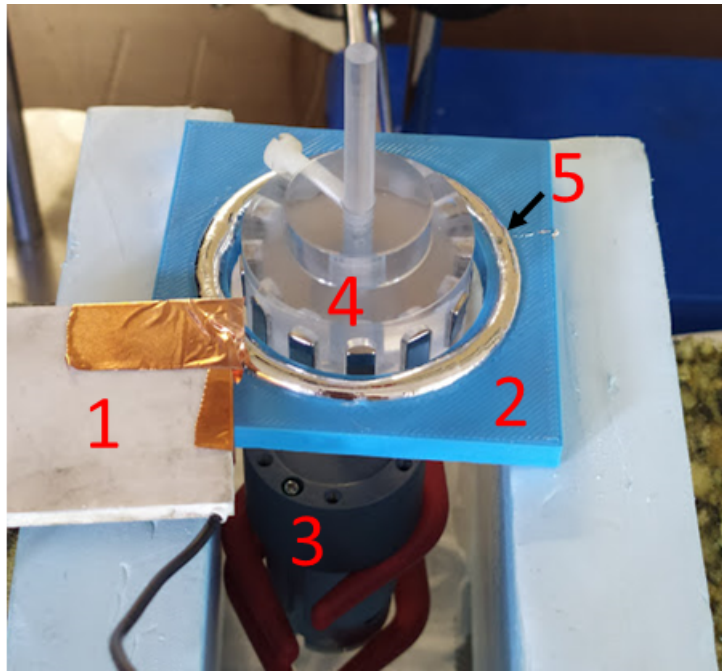
FIGURE 3.11: Experimental setup of the MHD induction cooling circuit; 1- Peltier with copper tape; 2- 3D printed PLA channel; 3- DC motor; 4- Rotor with embedded NdFeB permanent magnets; 5- Produced galinstan.

3.10.2 MHD DC conduction pump

The MHD conduction pump prototype is made of two concentrical electrodes made of copper and stainless steel respectively, and an array of 6 Nd-Fe-B permanent magnets with 20 x 20 x 2 mm dimensions, as can be seen in Figure 3.12. The permanent magnets

are set below the electrodes generating a field in the z direction. The magnetic field intensity as a function of distance of the magnets is represented on Figure 3.10. By now setting a potential difference between the electrodes we get a radial current passing through the fluid. The coupling between the radial current (at red in the figure below) and the magnetic field in the z direction (at green in the figure below) we get a tangential Lorentz force (at yellow in the figure below).
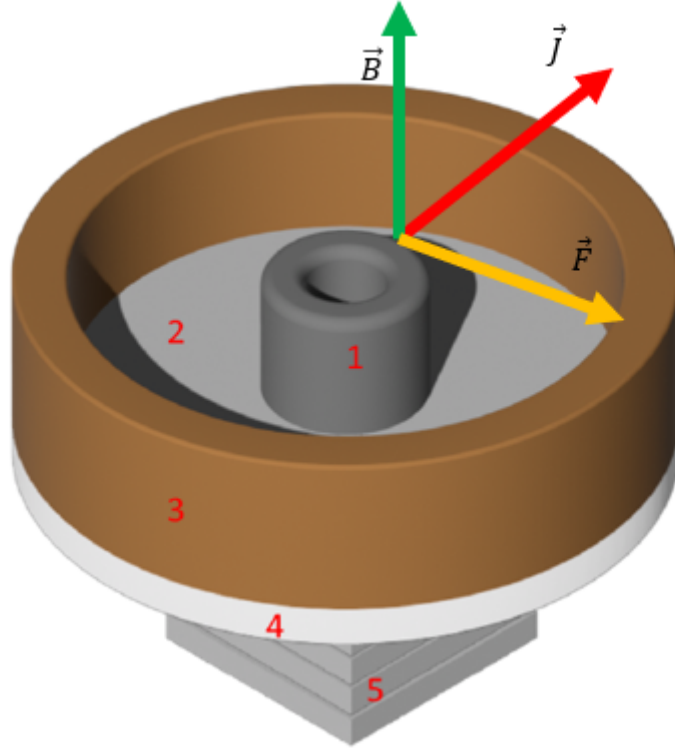
FIGURE 3.12: Experimental setup of the MHD DC conduction cooling circuit; 1- Stainless steel electrode; 2- Galinstan channel; 3- Copper electrode; 4- Plastic cover; 5- Array of squared NdFeB permanent magnets. Vectors of magnetic field (at green), current (at red), and Lorentz force (at yellow) are also represented.

Chapter 4

Results

4.1 Galinstan

Firstly, we did a morphology and elemental composition analysis of the produced Ga-In-Sn alloy with SEM-EDS, obtaining the spectrum represented in Figure 4.1. From that analysis was possible to determine the elemental composition of the sample, obtaining 68 wt% Ga, 22 wt% In, 10 wt% Sn. These results are in line with the intended galinstan alloy ($Ga_{68}In_{22}Sn_{10}$), however it should be noted that these measurements have an associated uncertainty of up to 5%.
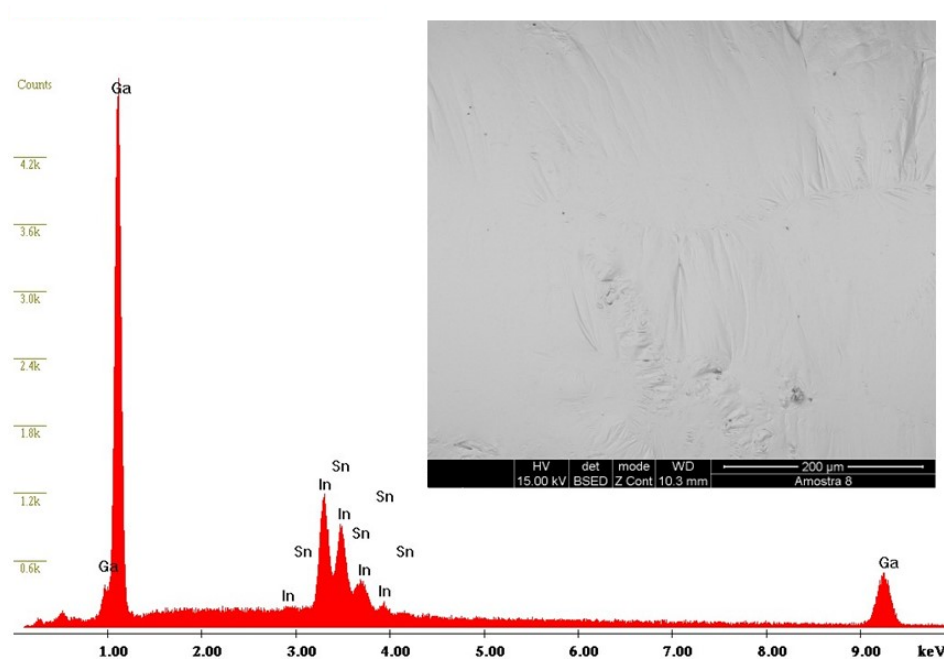
FIGURE 4.1: SEM-EDS spectrum of the produced Ga-In-Sn alloy as well as a SEM image of the liquid metal (inset).

It is important to note that the SEM-EDS measurement is made on a small section (few squared micrometers) of the total sample. For this reason, we cannot claim that the entire sample has the same determined Ga-In-Sn composition.

The produced alloy was then further characterized with DSC measurements. The thermogram corresponding to the heating and cooling of the liquid metal is represented in Figure 4.2. It is easy to notice right away that the melting temperature of the alloy (red curve) differs from its solidification temperature (blue curve). This is not uncommon in the literature and has been documented in several liquid metals, including galinstan [100] [101]. This phenomenon is called supercooling and is characterized by the solidification of the material at a temperature below its melting temperature, this difference in temperature is called the degree of supercooling, as defined in equation 4.1 where T_m is the melting temperature and T_s is the solidification temperature [102]. Physically, supercooling can be understood as an extra energy barrier to overcome originating from short-range ordering within the liquid[35].
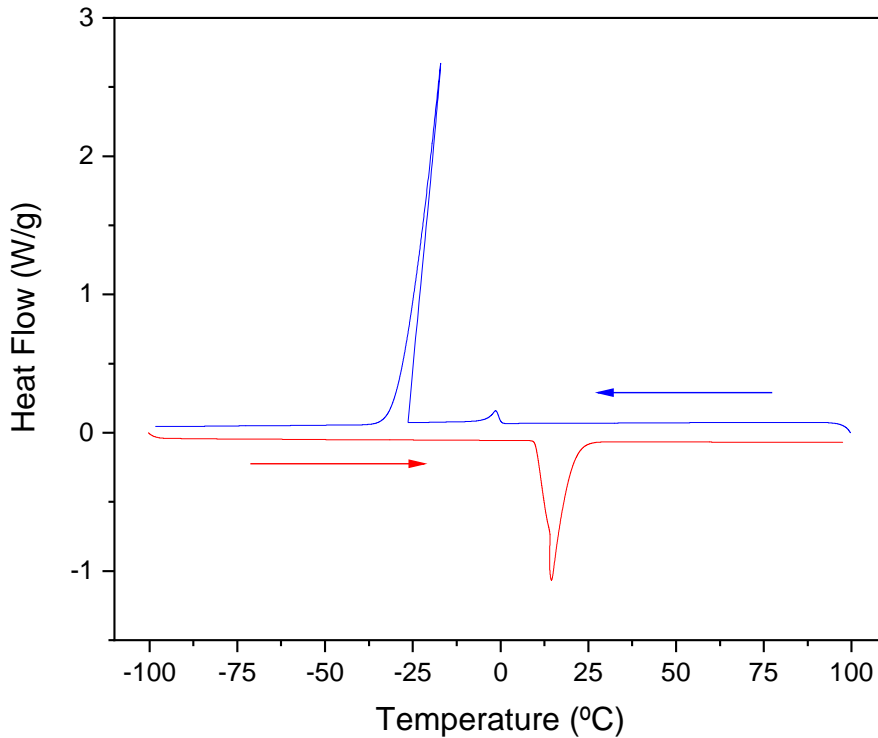
FIGURE 4.2: DSC thermogram of the fabricated Ga-In-Sn alloy from -100 °C to 100 °C, after being cooled from room temperature down to -100°C the sample is heated up to 100 °C (red curve) and then cooled down to -100 °C (blue curve).

$$\Delta T = T_m - T_s \tag{4.1}$$

From the literature, the melting temperature is reported both as -19 ℃ [35] and 11 ℃ [103], the first referring to its solidification temperature.

Analyzing now the curve corresponding to the heating protocol, we can see that there is a partial overlap of two peaks in a transition that onsets at T=9.8 ℃, as can be seen from the thermogram zoom in Figure 4.3. This leads us to the hypothesis that the melting of our alloy is not entirely homogeneous. MingJiang *et al.* [104] obtained for a Ga-In-Sn alloy (similar to galinstan in composition ($Ga_{69}In_{21}Sn_{10}$)) a melting peak with a shape similar to the one obtained in this work. Handschuh-Wang *et al.* [105] studied both galinstan and eutectic Ga-In-Sn, $Ga_{68.5}In_{21.5}Sn_{10}$ (EGaInSn), with DSC, for the EGaInSn he obtained a similar peak as the one in Figure 4.3. Regarding the galinstan, the authors obtained two separated melting peaks. Turning now to the melting point itself, we see that it is relatively lower than the 11 ℃ documented in the literature [103].
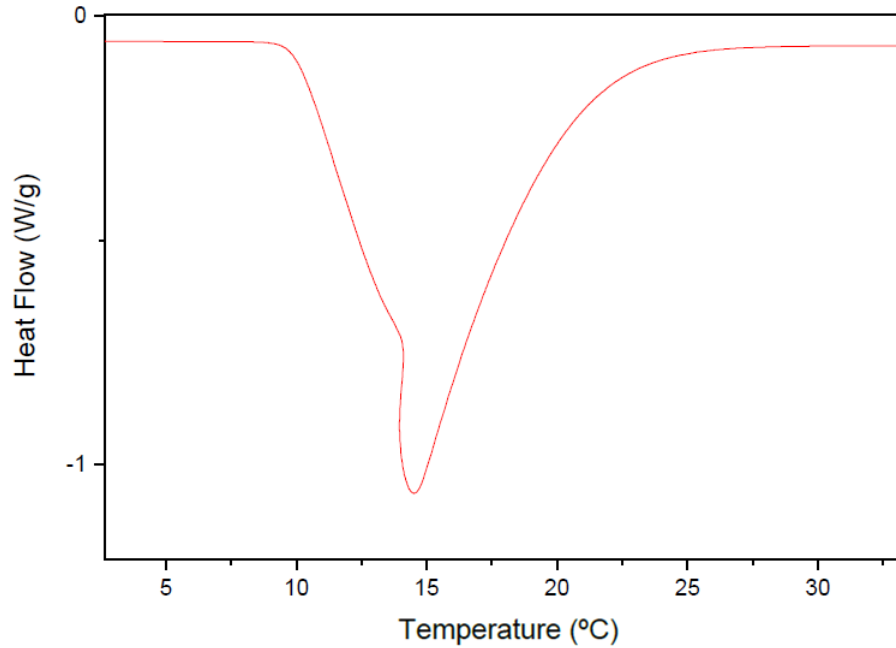
FIGURE 4.3: DSC thermogram zoom on the melting peaks observed during heating protocol.

Regarding the cooling protocol curve, we observe a more complex behavior. From the scan of Figure 4.2 we can identify two separate transitions, the first at 0.6 ℃ and the other around -26 ℃. A similar thermogram for the cooling ramp was obtained in [104], with a first small transition around 0 ℃ and a larger one at a lower temperature corresponding

to the actual solidification of the sample. The first peak, as explained in [106], is due to the development of a short-range order in one metallic phase. While the second peak represents the long-range solidification of the sample. It is worth noting that there is no consistent data in literature of the DSC of the solidification of galinstan. Some authors report the appearance of three peaks during the cooling protocol [70] [106], while others present similar results to those obtained in this work with only two peaks [104] [9]. This can somewhat be explained by the existence of different phases within the Ga-In-Sn alloy coming from different fabrication methods, thus altering the number of measured peaks as well as the position of the peaks in the thermogram. Comparing the value obtained for the solidification temperature with the reported value of -19 ℃ [106], we see that the value obtained is lower, possibly due to deviations from the expected composition of the alloy.

Other important thing to take into account regarding the position of the peaks is that it changes with different heating and cooling rates for example, the temperature of the melting peaks increases with increasing heating rate [107].

4.2   Magnetocaloric Particles

Using FullProf software, we carried out a LeBail refinement of the measured diffractogram. Figure 4.4 shows the fit obtained against the experimental pattern, as well as the statistics associated with it.
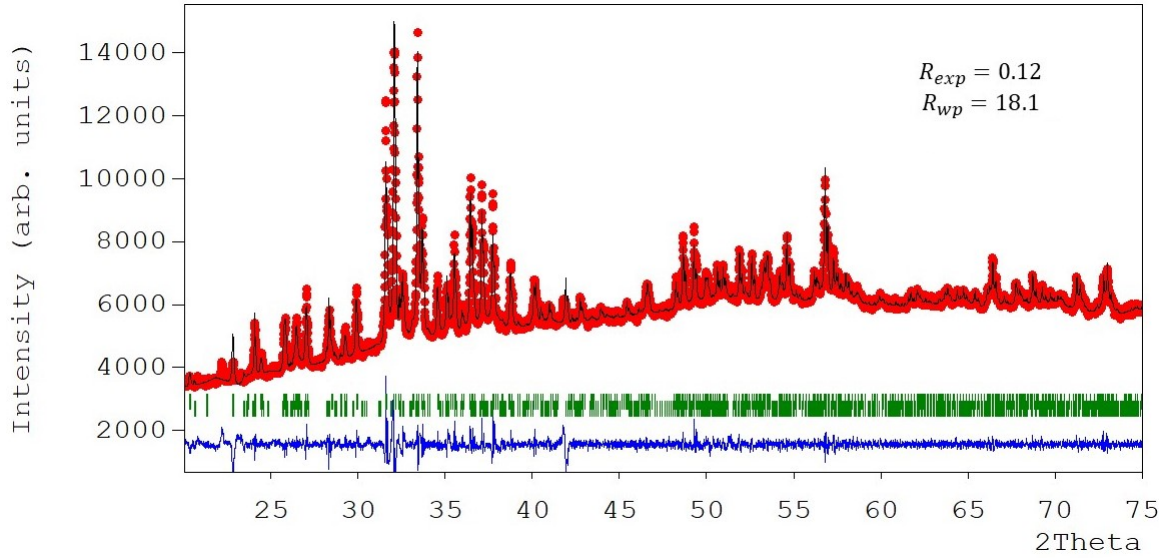
FIGURE 4.4: LeBail refinement performed on the XRD pattern of the fabricated $Gd_5Si_{2.4}Ge_{1.6}$ powder. The red points represent the observed intensities (y_{obs}), the black curve the calculated intensities (y_{calc}), the blue curve $y_{obs} - y_{calc}$ and the green one the Bragg position.

As we can see from the graphical analysis of Figure 4.4 the peaks are mostly all included in the fit. So despite the R_{wp} of our fit being large, this can be attributed to the low absolute intensity of our XRD pattern, which in turn increases the value of R_{wp}.

The fit included the Orthorhombic phase I (the expected phase for a sample with our stoichiometry) and the Monoclinic phase, from which it was possible to determine the percentages of these phases in the Gd-Si-Ge powder. The results were of approximately 75% of the Orthorhombic phase and 25% of the Monoclinic phase. Tabel 4.1 has the lattice parameters used on the LeBail refinement for both phases [108].

TABLE 4.1: Lattice parameters used for the Orthorhombic I and Monoclinic phases in the LeBail refinement.

	Orthorhombic I	Monoclinic
a ($\mathring{A}$)	7.5041 ± 0.0001	7.5884 ± 0.0004
b ($\mathring{A}$)	14.7749 ± 0.0003	14.7857 ± 0.0003
c ($\mathring{A}$)	7.7861 ± 0.0001	7.7849 ± 0.0003
α (º)	90	90
β (º)	90	90
γ (º)	90	92.750 ± 0.005

The MCPs were then analyzed with SEM, Figure 4.5a) shows the resulting SEM micrograph of the powder and an inset with the EDS spectrum. The micrograph shows, as expected, a non-uniform distribution of particle sizes at the micrometer scale. From the

EDS analysis we obtained an atomic percentage of Gd 60%, Si 24% and Ge 16%. Comparing this composition with the expected 56:27:18, we can see that the values obtained with a maximum associated uncertainty of 5% cover the expected composition.

Using the ImageJ software, we analyzed the sizes of the particles in the figure below, obtaining the following histogram. A lognormal fit was then performed to the data, with a mean length of particles of 1.08 μm as can be seen in Figure 4.5b).
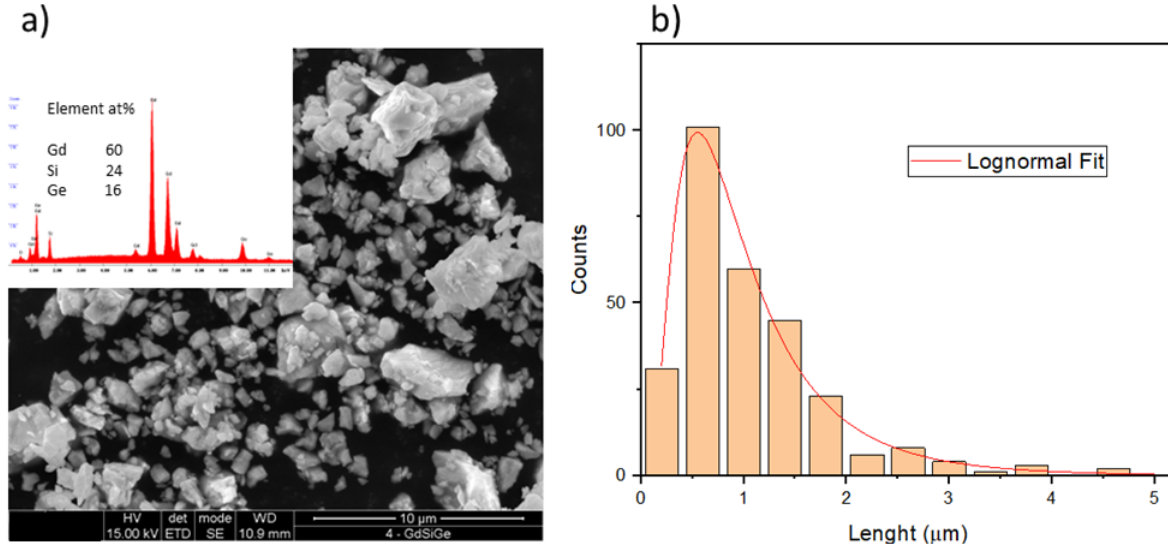
FIGURE 4.5: a) SEM micrograph of the produced Gd-Si-Ge powder. Inset image shows the EDS spectrum and atomic percentages obtained for the alloy. b) Histogram of the particle length distribution with a lognormal fit.

Regarding the magnetic characterization of the Gd-Si-Ge powder, we began by determining the T_c. For that, we measured the isofield (1000 Oe) magnetization as a function of temperature curves from -268.2 to 100.9 ℃ for cooling and heating, respectively, represented in Figure 4.6. From the analysis of the data, we see that the material undergoes a single magnetic phase transition which assures us that we have a material mainly composed of a single phase, as proven by XRD measurements in Figure 4.4. Despite having 25% of Monoclinic phase, it is not unusual for this alloy not to present two magnetic transitions in the M(T) curves [109].

In order to estimate the T_c we can determine the temperature at which the derivative of magnetization as a function of temperature is maximum. From the inset of Figure 4.6 we can see that the determined T_c was 33.8 ℃ and 34.1 ℃ for cooling and heating respectively. The produced particles have, as expected, a magnetic transition at slightly above room temperature, which is required as we intend to fabricate a room temperature heat dissipator based on thermomagnetic convection. This alloy has a magnetic transition

referenced at 32.9 ℃ [108], since the T_c calculated is practically 1 ℃ higher, this small difference can be attributed to the fact that the measurements were taken on different machines and under slightly different measurement protocols and to slight stoichiometry differences.
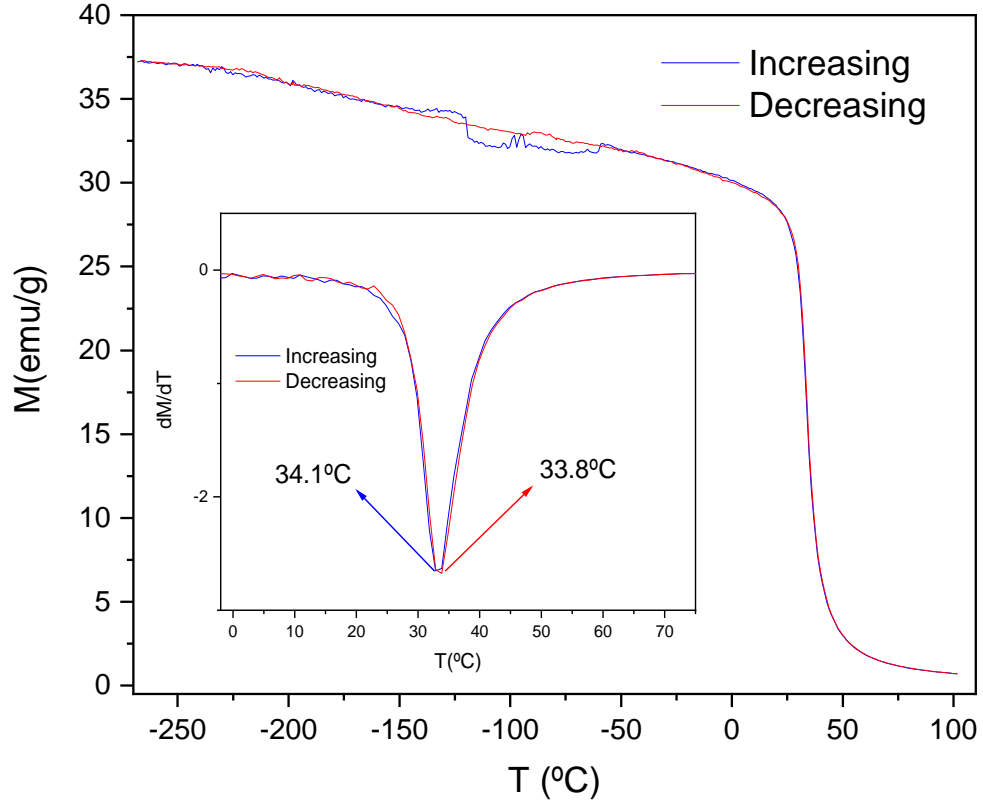
FIGURE 4.6: Isofield (1000 Oe) magnetization as function of temperature for a cooling and heating protocol, red curve for cooling and blue curve for heating. Inset image represents the calculated magnetization derivative in order of temperature as well as the determined values of T_c for cooling and heating.

In order to quantify the MCE of our sample, we began by measuring isothermal M(H) curves. The curves were measured for temperatures between -3.2 and 66.9 ℃ with a step of 2 ℃, under magnetic fields from 0 to 7 T. Figure 4.7a) shows the measured M(H) curves, where in blue we have the curves in which the material is in its ferromagnetic state, while the red curves represent the M(H) curves of the material in its paramagnetic state.

Using equation 2.2, we obtained the graph in Figure 4.7b) that represents the entropy variation of our material as a function of temperature for a magnetic field of 7 T. The entropy change of the material peaks at -9 $Jkg^{-1}K^{-1}$ for a temperature of around 36.9 ℃.

Filipa Furriel *et al.* [70], obtained for the same alloy an entropy change of -6 $Jkg^{-1}K^{-1}$ at 34.9 °C for a magnetic field change of 5 T. Calculating the change in entropy with the same data but for a change of 5 T, we obtain approximately -7.2 $Jkg^{-1}K^{-1}$, which is higher than that obtained in [70]. Since there are several factors that influence the entropy variation of the material, such as particle size [110], microstructure [111], induced strain [112], chemical disorder, we cannot conclude that this difference is due to changes in the expected stoichiometry.
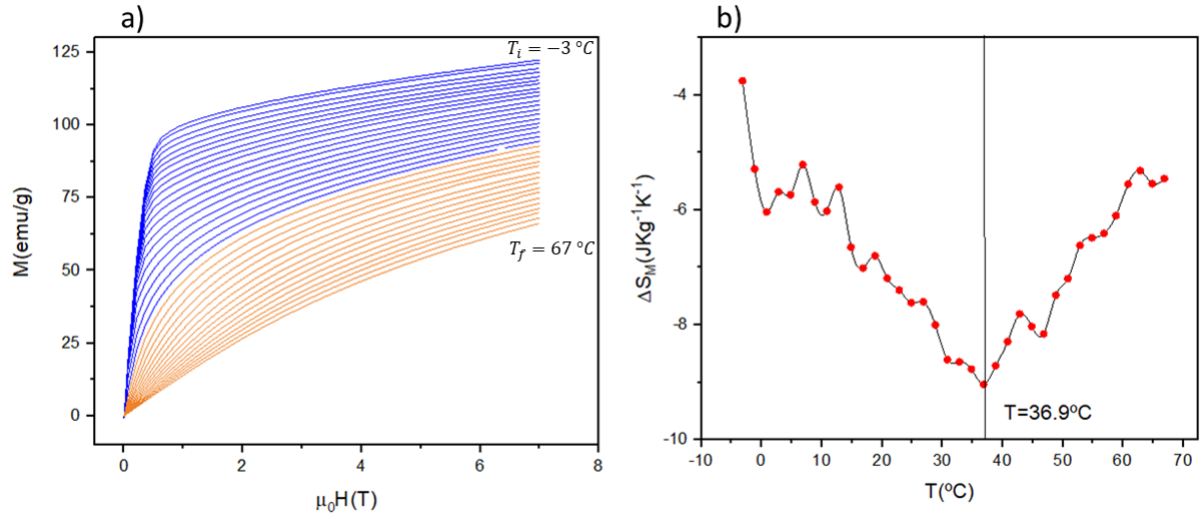
FIGURE 4.7: a) Isothermal M(H) curves measured around T_C , blue and red curves corresponding to a temperature below and above T_C respectively. b) Calculated entropy variation as a function of temperature connected with an spline.

The magnetic phase transition was further analyzed by DSC. Figure 4.8 shows the obtained thermogram from which we can see a transition at around 30 °C for both heating and cooling curves. This difference in temperature compared to the temperature obtained by the SQUID measurements can be explained by the fact that the DSC measurements were taken at zero magnetic field and under different heating and cooling protocols. In the heating curve we see that upon the ferromagnetic to paramagnetic state, the sample absorbs heat. As for the cooling curve, we observe an exothermic process characterized by the release of heat by the sample as it goes through the paramagnetic to the ferromagnetic state.
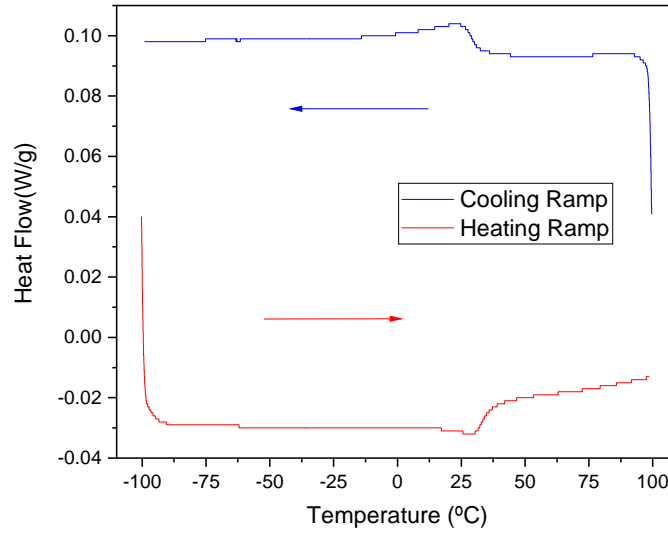
FIGURE 4.8: DSC thermogram zoom on the melting peaks.

4.3 Magnetic fluid

After the production of the mixtures of galinstan with $Gd_5Si_{2.4}Ge_{1.6}$ powder we began to test their magnetic actuation upon the approximation of a permanent magnet. A video of the results can be consulted on the link in the footer below [*]. As expected, the magnetic actuation has an upward qualitative trend with the increase in the percentage of MCM incorporated into the galinstan.

The mixtures were analyzed using SEM-EDS in order to visualize the distribution of particles in the galinstan liquid matrix. Figure 4.9 shows the results obtained from the SEM-EDS analysis of the mixture with 6wt% of MCM. The micrograph shows the matrix of galinstan with microparticles of MCM at its surface, confirmed with the EDS spectrums identified as Z1 and Z2 respectively.

It is also important to note right away that the particle distribution within the galinstan is not uniform which was to be expected, since the size distribution in the powder was large. The sample is composed of mainly galinstan with some clusters of magnetocaloric particles.

---

[*] https://drive.google.com/drive/folders/19Ex9wHFbvNbCeuqdJOyJGKzo9RFmqded?usp=sharing
Videos showing the magnetic actuation of the three produced mixtures
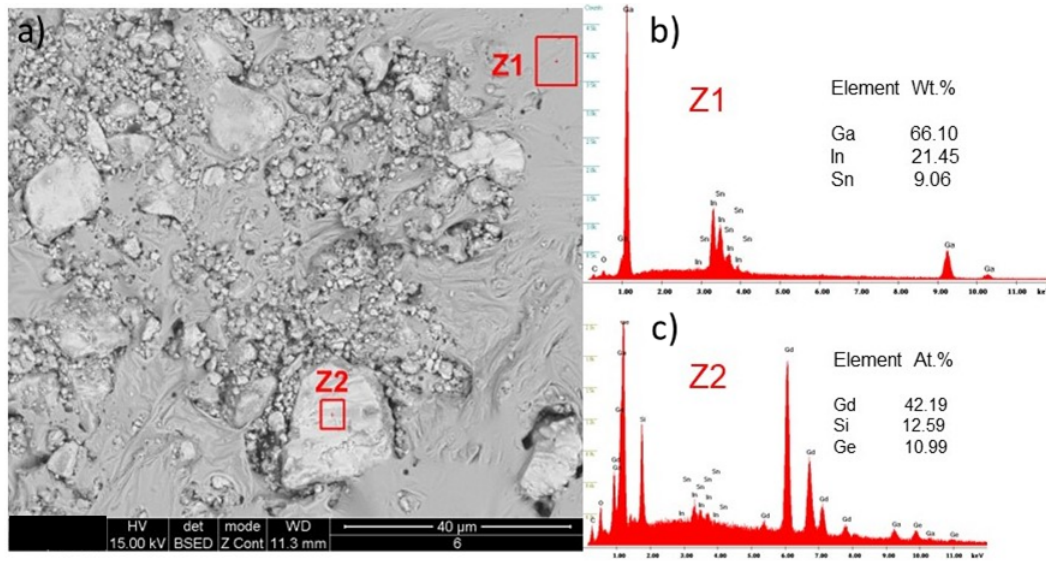
FIGURE 4.9: a) SEM image of the produced mixture of galinstan with 6wt% of micropar-
ticles of $Gd_5Si_{2.4}Ge_{1.6}$; b) EDS spectrum of element Z1; c) EDS spectrum of element Z2.

The mixtures were then magnetically analyzed with SQUID. Starting by measuring
the magnetization as a function of temperature, we obtained the results presented in Fig-
ure 4.10. We can see that we still have a singular magnetic phase transition, which in-
dicates that no new magnetically ordered phases are generated from our Gd-Si-Ge alloy
when it is mixed with galinstan.

Through the analysis of the magnetization derivative as a function of temperature,
we were able to estimate the T_C of our mixture, as seen in the inset image of Figure 4.10.
Obtaining a T_C of 33.5 ℃, which correlates nicely with the values obtained for the Gd-Si-
Ge powder. This further reinforces the idea that, at least in the short to medium term (at
least 3 months), galinstan does not alter the properties of the magnetic transition of our
MCM. It is also worth noting the presence of a small artefact in the graph at T = -16.2 ℃
which could be due to the solidification of the galinstan.
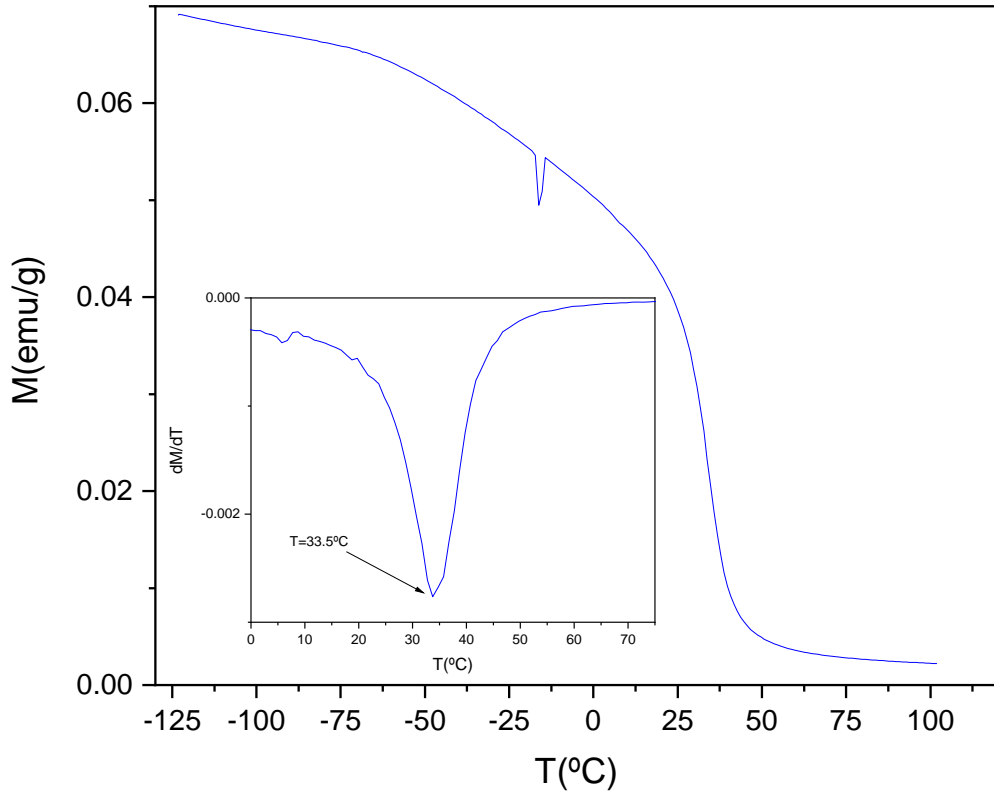
FIGURE 4.10: Isofield (1000 Oe) magnetization as function of temperature for the cooling of a mixture of galinstan with 2 wt% of $Gd_5Si_{2.4}Ge_{1.6}$. Inset image represents the calculated magnetization derivative in order of temperature as well as the determined value of T_C.

The nominal loadings of magnetocaloric particles in the respective mixtures (2 wt%, 4 wt% and 6 wt%) have been mentioned throughout this thesis. However, it is to be expected that the "real" values are smaller than the nominal ones because at the end of the transfer of the mixtures produced into eppendorfs, particles were visible in the mortar along with the layer of oxidized galinstan left behind.

In order to quantify the actual loading in the mixtures, we again performed SQUID measurements of our samples. The loadings were determined by comparing the saturation magnetization M(H) curves at T = -263.2 ºC of our alloy powder and the respective mixture under study. Figure 4.11 a) shows the M(H) curve measured at -263.2 ºC for the Gd-Si-Ge powder and Figure 4.11 b) the M(H) cuurve measured for the sample of the galinstan mixture with a nominal loading of 2 wt%. First, a linear fit was made at the

high-field region of the M(H) curves in order to determine the slope. The slope potentially associated with minor fraction of paramagnetic phase was then subtracted from the M(H) curves to remove the paramagnetic component in order to determine the saturation magnetization, the resulting curves are shown in red in Figure 4.11. In this way we were able to extract the values of the saturation magnetizations, obtaining for Gd-Si-Ge powder a value of approximately 196 emu/g. By dividing the values of the non-normalized saturation magnetization obtained for the various mixtures by the value of the saturation magnetization of the Gd-Si-Ge powder, we obtain an estimate of the mass of Gd-Si-Ge present in the sample. Now to determine the loading of MCM in the sample we only need to divide this value by the total mass of the sample.
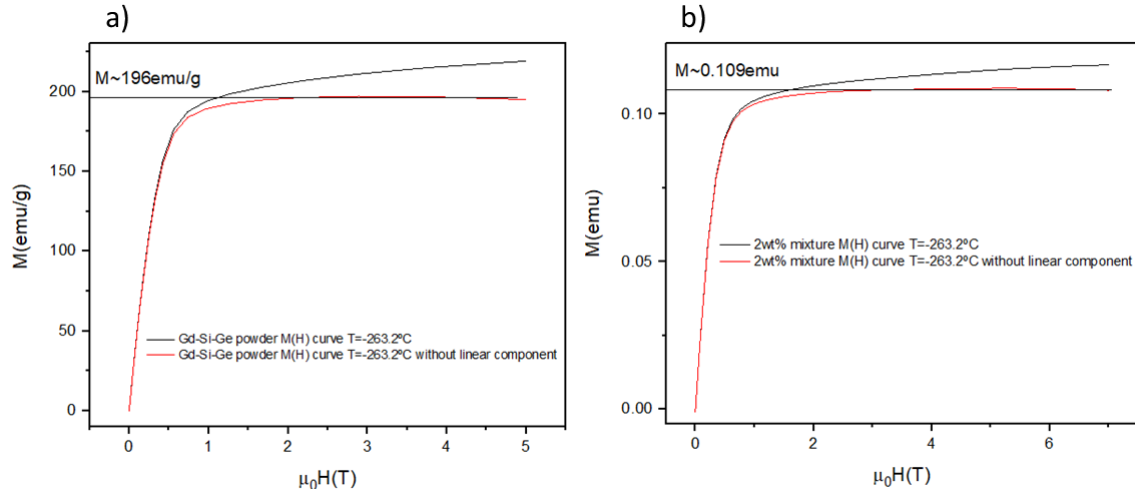
FIGURE 4.11: M(H) curves at T = -263.2 °C for the - a) Gd-Si-Ge powder; b) galinstan mixture with a loading of 2%. The curves at black represent the original measured curves while the red ones stand by the curves without the linear component.

The results of the loadings of the different mixtures are shown in Table 4.2. Initially, three M(H) measurements were taken, one for each mixture. However, as can be seen in the figure below, the loading obtained for the 2 wt% sample is the highest among the three, contrary to the expected. As we saw above, the magnetic actuation of the samples to the approach of a permanent magnet was found to be stronger as expected due to the higher loading. The results obtained are therefore a potential indicator of the non-uniformity of our samples, as seen in the SEM images. For this reason, we decided to make a new set of measurements on the different samples from each of the three mixtures in order to highlight potential loading variability within the mixture, represented in the last row of the table below.

Comparing the two sets of measurements, we can see that there is considerable variability between the two. In the second set, the loading determined for 6 wt% is three times larger compared to the previous one, while the other two loadings drop their value to almost half of the previous one. These results confirm the non-uniformity of our mixtures, so care should be taken on using this method to estimate the loading in the mixtures.

This lack of uniformity comes from several factors, the most obvious being the non-uniform incorporation of the particles during the fabrication of the mixtures. Another factor is the effect of exposing the sample to a magnetic field, because when ferromagnetic particles are attracted to the magnetic field, they eventually form clusters of particles due to dipolar interactions between particles. Therefore, removing the magnetic field does not necessarily result in the particles returning to their original position in the liquid matrix.

Another important feature to take away from the results is that all the loadings calculated are far below the expected loading. This can be explained, as mentioned above, by the particles that are still visible in the mortar that have not been incorporated during the fabrication of the mixtures. However, this is not the only factor responsible for the reduction in real loading. Some of the particles in the mixture are lost on the walls of the eppendorf where they are stored, as well as in pipettes that are used to transport the mixtures and prepare samples. In the future this can be reduced by storing the mixtures on containers filled with an acidic solution.

TABLE 4.2: Calculated loading percentages for the two sets of measurements of the three fabricated mixtures.

Calculated Loading(%)	Measurement Number	2wt%	4wt%	6wt%
	1	0.24	0.04	0.12
	2	0.14	0.03	0.35

The mixture was further analyzed using DSC, Figure 4.12 a) and b) show the comparison between the thermograms obtained for the galinstan above and the mixture of galinstan with 6wt% of the Gd-Si-Ge alloy for heating and cooling protocols respectively.

Regarding the melting of the sample, we again detect a peak formed by the overlapping of two peaks. As for the relative position of the peaks, we observed that the melting of the mixture occurs at a slightly lower temperature. Now looking at the cooling protocol, we still have two peaks that occur at slightly higher temperatures. These differences between the positioning of the peaks in the two thermograms for the galinstan and the magnetic fluid can be attributed to the fact that we are dealing with slightly different phases of galinstan in the two samples and not so much to the particles in the mixture.
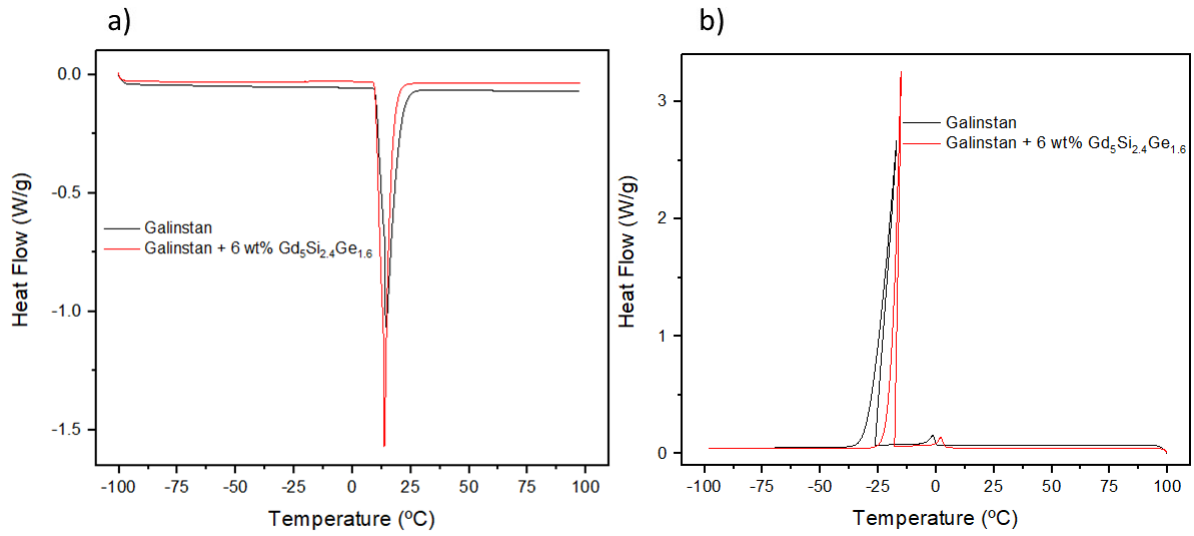
FIGURE 4.12: DSC thermogram of galinstan at black and of a mixture of galinstan and 6wt% of $Gd_5Si_{2.4}Ge_{1.6}$, of - a) heating ramp; b) cooling ramp.

In order to observe the magnetic transition of Gd-Si-Ge in our mixture, we zoomed in on the thermogram in the vicinity of the Curie temperature, as can be seen in Figure 4.13.

A comparison of the curves for the mixture and Galinstan shows no magnetic transition. This is most likely due to the low loading of magnetocaloric particles in the mixture, a similar result was obtained in [70].
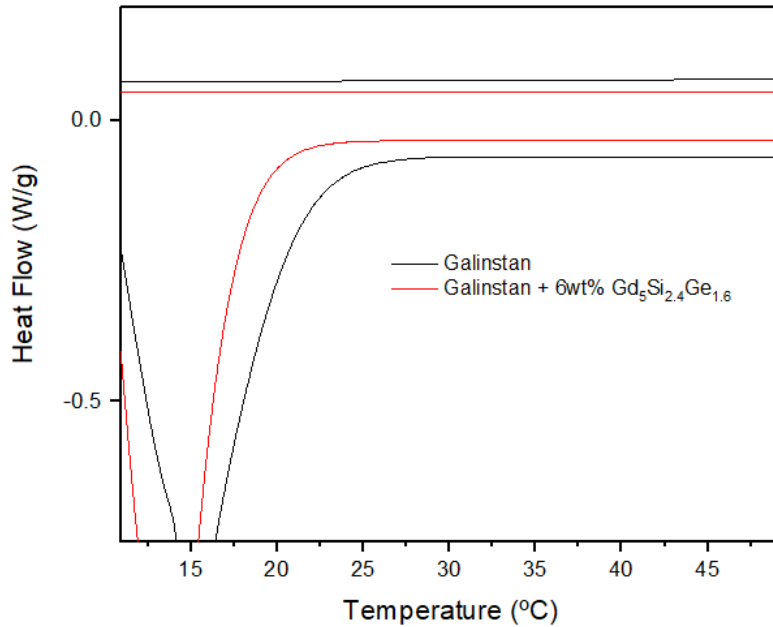
FIGURE 4.13: Zoom of the DSC thermogram in the vicinity of the Curie temperature of Gd-Si-Ge. The black curve represents the measurements in galinstan, while the red curve represents the mixture with 6% loading.

4.4 Thermomagnetic convection heat dissipator

We started by testing the prototype schematized in Figure 3.9 with a magnetic field intensity on the channel between 0.18 and 0.10 T with a temperature gradient of around 7 ºC, but we were unable to observe any movement of the mixture. However, as the fluid has a high reflectivity, it turns out to be quite complicated to observe small flows of the mixture in the channel. For this reason, in order to really check whether there is any flow of the mixture in the heat sink channel, we used the thermal camera to record the thermal profile of our channel during the heating of the fluid in the vicinity of the Peltier with and without the presence of the permanent magnets. Therefore, if there is a flow of the mixture the heat dissipation should occur in a faster way than in the case where there is no flow of our mixture, thus we would expect to find a discrepancy between the two thermal profiles. Figure 4.14 shows the thermal profiles obtained for the cases without (thermal profile a)) and with permanent magnets (thermal profile b)) 3 minutes after the Peltier was turned on.
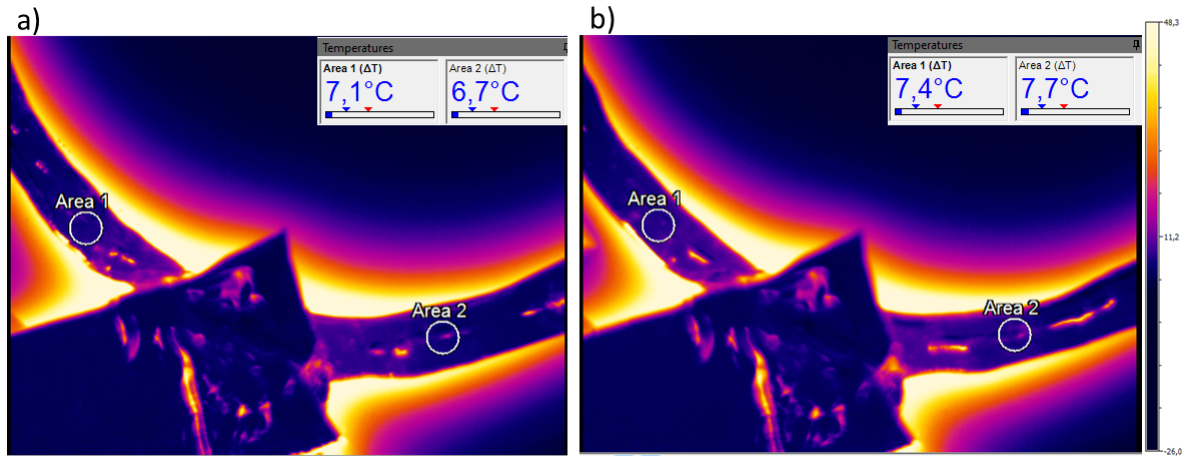
FIGURE 4.14: Thermal profiles recorded while heating the mixture with a Peltier - a) without and b) with the presence of permanent magnets at t = 3 minutes. The temperatures displayed for the measuring areas correspond do the mean value of all temperatures inside the area. It is important to note that a background corresponding to the profile at t = 0 s (when the Peltier was switched on) has been removed from these profiles, so the temperatures shown correspond to a temperature variation in regard to the initial temperature.

From the analysis of the thermal profiles, it is not possible to identify any relevant discrepancies between them so we conclude that there is no significant movement of the mixture in the channel. This can be explained by a number of factors. On the one hand, unlike the ferrofluids normally used in these applications with nanoparticles dispersed in water, our fluid is made up of a galinstan matrix which has a viscosity more than

twice as high. For this reason, the pumping force required to obtain a fluid flow of the same order of magnitude must be higher. This pumping force depends on several factors, including the loading of particles mixed in the fluid. As analyzed above, the fabricated mixtures have an actual loading well below what was expected, which may be one of the reasons why the prototype did not work. At the end of the tests, the mixture was collected with a pipette into an eppendorf, and it was found that its magnetic actuation was noticeably weaker compared to its initial state, thus suggesting that a portion of the particles had been deposited at the bottom of the channel or had adhered to the channel walls during the prototype testing process. This, combined with the non-uniformity of our fluid, presents problems for the continued operation of the heatsink. Since the mixture would be loaded less and less, this would lead to a lower pumping force and the eventual cessation of movement.

On the other hand, the high surface tension of the fluid combined with the small diameter of the channel presents yet another barrier to the start of the mixture's movement.

At this point in the thesis, it was necessary to make a decision: continue with the concept of pumping the fluid through thermomagnetic convection and work on improving the uniformity of our fluid (testing new fabrication methods), increasing the effective loading of particles in the fluid (using particles of other materials). Or change the paradigm to an alternative pumping method, in this case MHD. In the end, we decided to change the paradigm and now instead of relying on the loading of particles in the mixture to pump it, we now rely on the fact that our fluid has a high electrical conductivity.

4.5   COMSOL simulations - MHD induction pump

We start by doing a stationary study of the geometry schematized in Figure 3.8 from which we obtain the magnetic field distribution in our geometry at steady state (the frequency of our rotor is zero). This data is then used as the initial conditions for our time-dependent study. It is important to note that as the system is stationary there is no variation in our magnetic field, so there is no current generation in our fluid and consequently there is no pumping force being exerted on the fluid, so its velocity is zero.

Figure 4.15 a) shows the magnetic flux norm and the magnetic field lines at t = 0s for a frequency of 1 Hz from the time dependent study.
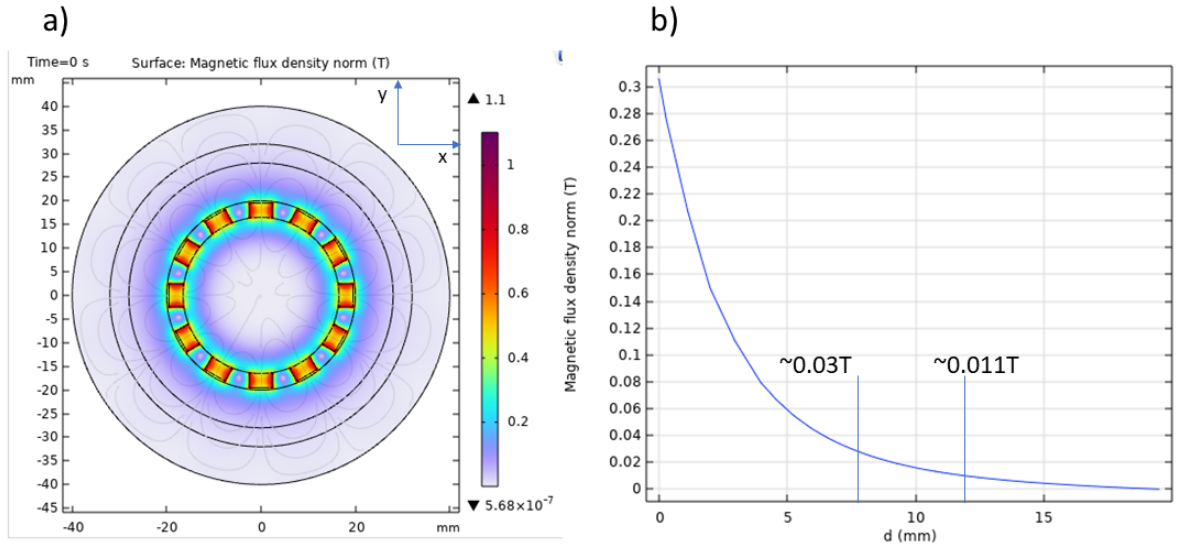
FIGURE 4.15: a) Magnetic flux density norm (surface plot) and magnetic field lines simulated with the time dependent study at t = 0 s for a rotor frequency f = 1 Hz; b) Magnetic field intensity in the y direction at t = 0 s, starting from a position 1mm apart from the surface of the permanent magnet. Ther vertical lines show the magnetic field intensities on the mini-channel boundaries.

Figure 4.15 b) shows the magnetic field intensity as a function of distance from 1 mm apart of the surface of the permanent magnets to the limits of the geometry. We can see that the magnetic field magnitude on the channel goes from 0.03T down to 0.011T at the farthest boundary of the magnets. In order to compare these simulated values with the real ones, we used a Gauss meter to obtain the data in Figure 4.16. It can be seen that the values obtained from the simulation are considerably higher than those obtained experimentally, namely the magnetic field intensity on the channel that now experimentally varies between 0.01 and 0.005 T. This difference in magnitudes is largely due to the experimental conditions not being ideal, unlike the ones on the simulation.
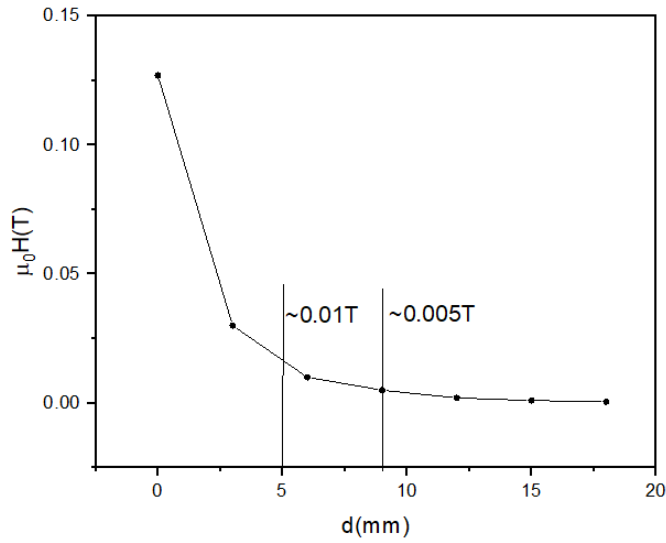
FIGURE 4.16: Magnetic field intensity of the permanent magnet rotor measured with a Gauss meter as a function of distance, the first point corresponding to the Gauss meter in direct contact with the permanent magnets, the vertical lines represent the magnetic field on the galinstan channel walls.

As we already have a variation in the magnetic field over time in the time-dependent study, we are already inducing, according to Lenz's law, out-of-plane current loops in our channel in order to cancel out the field variation. The Figure 4.17 shows the distribution of the current density norm induced in our galinstan (graph a)), it is important to note that vectorially this current consists of out-of-plane loops and the current density evolution over time in the middle of the mini-channel (graph b)).
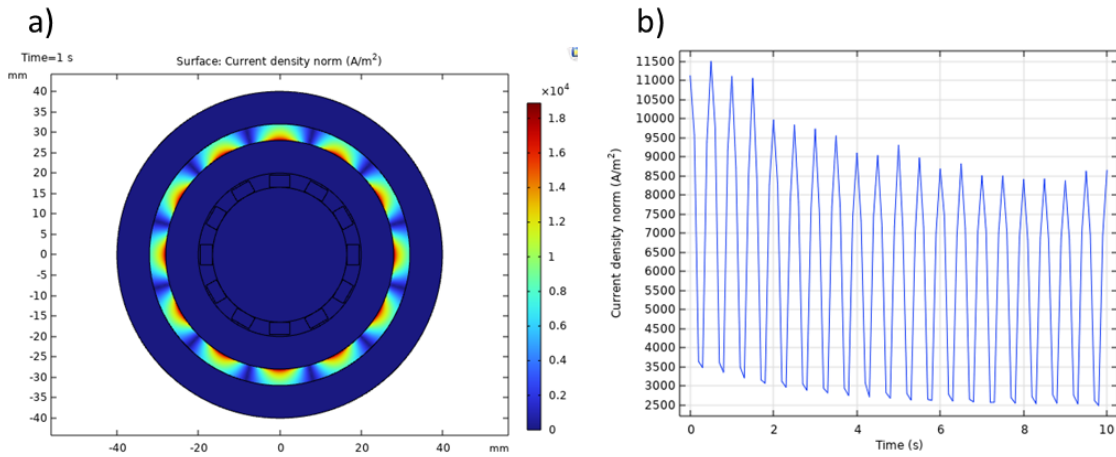
FIGURE 4.17: a) Induced current density norm distribution on the galinstan mini-channel at t = 1 s and f = 1 Hz; b) Induced current density norm as a function of time in the middle of the mini-channel at f = 1 Hz.

Analyzing the evolution of the induced currents we see a decrease in their maximum over time until they stabilize, this is due to the increase of galinstan's velocity until it

reaches its equilibrium point.

The coupling of the magnetic field with the induced currents results in the appearance of a Lorentz force perpendicular to both stimuli according to the equation 2.5. Figure 4.18 a) and b) show the force distribution in the channel, as we can see the force is not just tangential, forming loops along the channel. Later on, we will analyze if this force profile can cause the fluid backflows in certain parts of the channel.
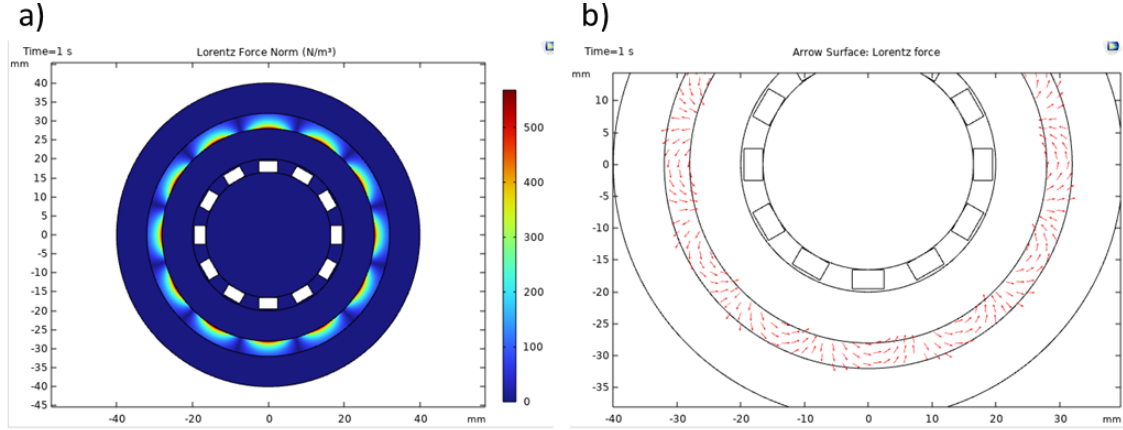
FIGURE 4.18: a) Induced Lorentz force distribution in the galinstan channel; b) Arrow surface of the induced Lorentz force in the channel.

By solving the equations for laminar flow, we can now extract the velocity profiles of the galinstan over time, as shown in the Figure 4.19.

As the rotor is moving at a constant rotational frequency, the induced current and consequently the Lorentz force will oscillate at a frequency equal to the oscillation frequency of the magnetic field. Therefore, in terms of fluid velocity, it is expected that it will start to increase approximately linearly as if it were under the application of an effective Lorentz force. Reaching its saturation value after the prototype has been running for some time.
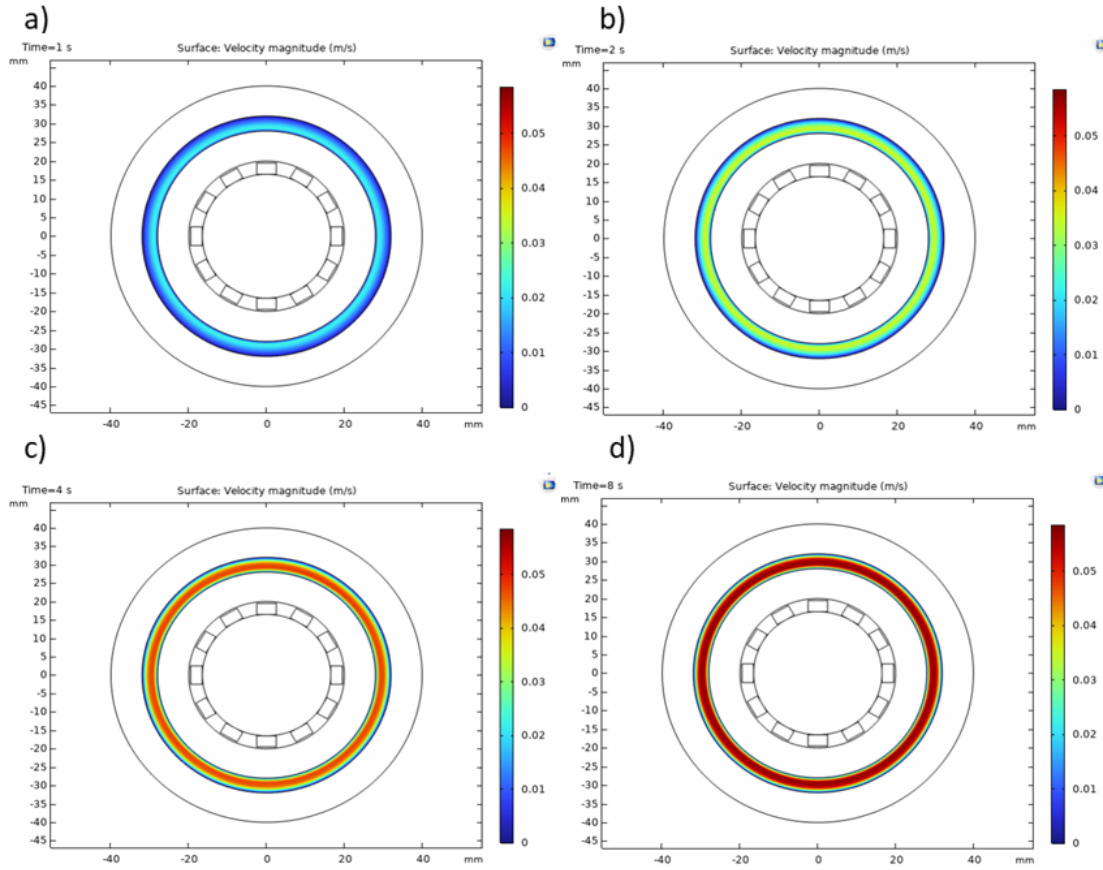
FIGURE 4.19: Simulated velocity profiles along the channel for f = 1 Hz at - a) t = 1 s; b) t = 2 s; c) t = 4 s; d) t = 8 s.

In order to study the evolution of the galinstan's velocity over time, we placed a velocity probe in the middle of the channel of our simulation. Graph a) in Figure 4.20 shows the evolution of the velocity at this point for various frequencies over a time interval of 10 s. As expected, we observe an approximately linear increase in velocity in the initial moments, until it begins to relax towards its equilibrium value.

We can now study the evolution of the magnitude of the equilibrium velocity as the rotor frequency increases. As can be seen in graph b) of Figure 4.20, there is an approximately linear increase in saturation velocity with frequency. This can be explained by the linear increase in induced current with frequency for low frequencies [113], which in turn results in a consequent increase in induced force and fluid velocity.
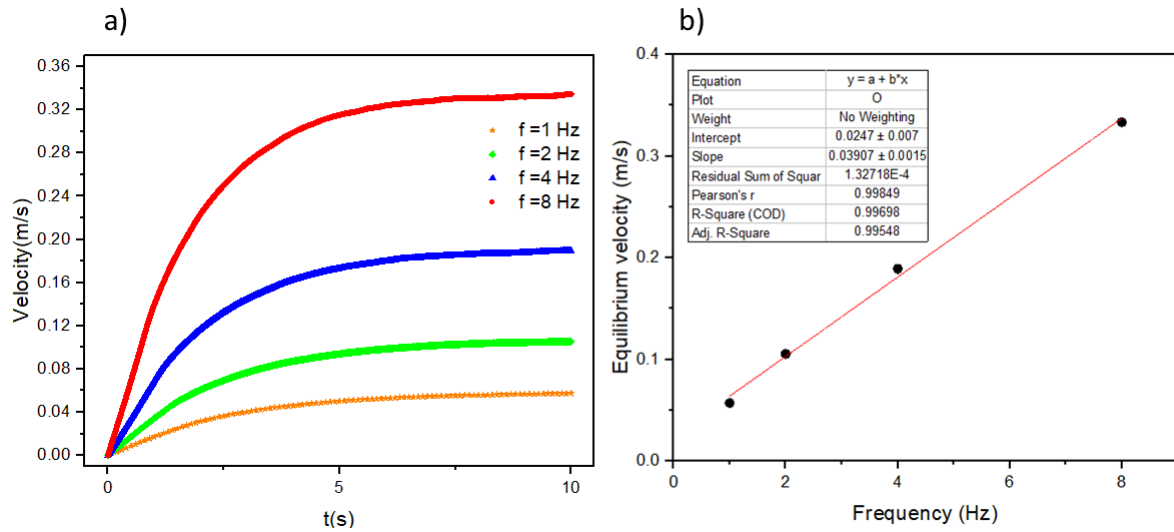
FIGURE 4.20: a) Velocity in the middle of the galinstan channel as a function of time for different values of rotor frequency; b) Equilibrium velocity as a function of rotor frequency.

In order to check whether we had galinstan backflow in our channel, we plotted the graph in the Figure 4.21. As can be seen from the directions of the arrows, the flow of galinstan is unidirectional, so there is no backflow.
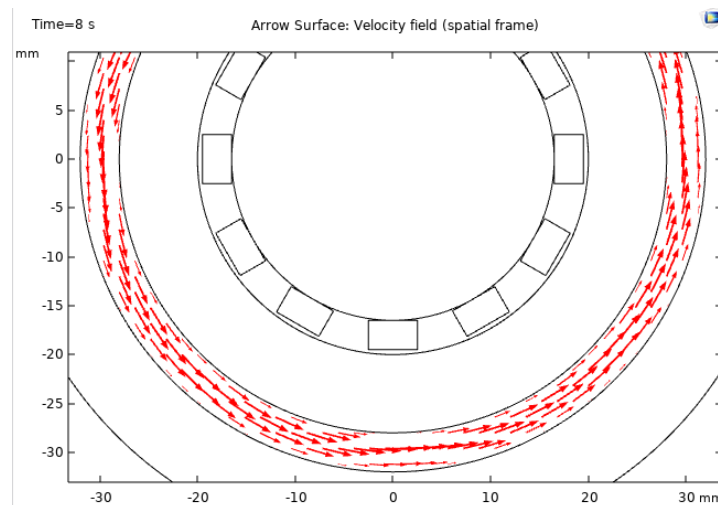
FIGURE 4.21: Arrow surface of the galinstan velocity at t = 8s.

Animations of the performed simulations can be consulted in the link on the footer below.[*]

---

[*]https://drive.google.com/drive/folders/1faQTag0BTC5ng45_rnsk6BQ_gsRsBxgR?usp=sharing
Animations of the the COMSOL time dependent study

4.6   MHD pumping

We started by testing the prototype from Figure 3.11, and it was not possible to observe any movement of the fluid upon the rotation of the permanent magnets. The measured magnetic field on the channel was between 0.01T and 0.005 T which is considerably lower than obtained in the simulation, also the rotor frequency was of approximately 2.7 Hz. Due to the galinstan's high reflectivity, it would be difficult to observe small flows at the naked eye, so we used again the thermal camera.

Figure 4.22 shows the thermal profiles of the galinstan channel after 1 and 3 minutes of movement of our rotor. From the analysis of the profiles, it is not possible to detect any significant fluid flow, but we do visualize that the fluid gets hotter, most likely due to Joule heating caused by the induced currents.
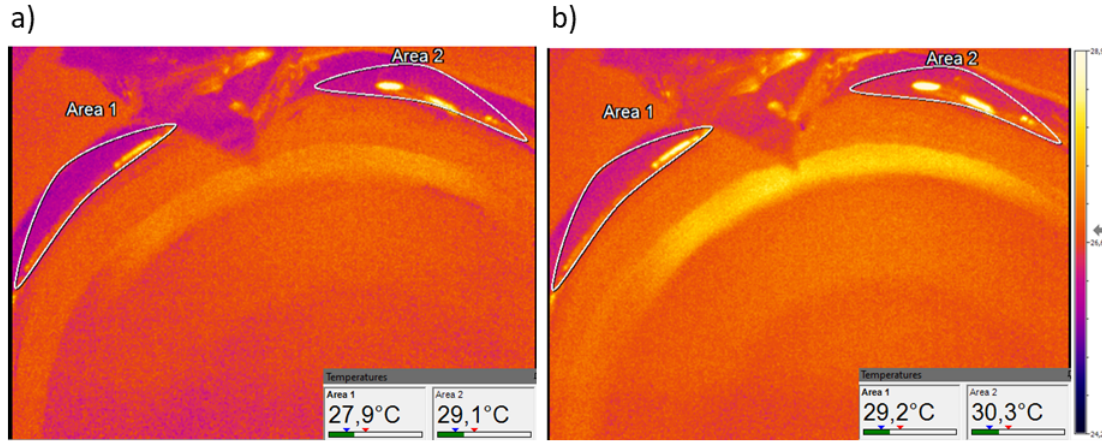
FIGURE 4.22: Temperature profiles of the galinstan channel recorded after 1 (graph a)) and 3 minutes (graph b)) of the start of the rotor movement. The temperature of the measuring areas corresponds to the maximum value of temperature recorded in the respective area.

The failure of the prototype to function in contrast to the COMSOL simulations can be understood by several factors: i) The COMSOL model does not take into account the surface tension of the fluid, which together with the small diameter of the channel presents a barrier to the start of fluid movement; ii) A part of the currents induced in the galinstan will result in Joule heating instead of coupling with the magnetic field to induce a Lorentz force and the experimental magnetic fields are considerably lower than those simulated; iii) The COMSOL model is inherently 2D, so it does not take into account out of plane magnetic fields whose temporal variation will generate currents and consequently forces

in non-trivial directions. These in turn will reduce the magnitude of the galinstan pumping force in the channel.

For these reasons, the induced pumping force will have to be increased to ensure that the prototype works. This force depends on several factors, such as the magnitude of the magnetic field and the induced currents. In a future iteration these factors can be improved in various ways: the magnitude of the magnetic field can be increased by using a higher mass of magnets and reducing the distance from the magnet rotor to the galinstan channel. As for the magnitude of the induced currents, this increases linearly with the oscillation frequency of the magnetic field. As there are limitations on the frequencies achievable with a small DC motor, increasing the frequency can be achieved by using a greater number of permanent magnets in order to increase the periodicity of the magnetic field distribution. If the frequency achieved is not sufficient, the use of coils would allow the magnetic field to switch much faster, resulting in a higher magnitude of induced currents.

In order to check the galinstan's behavior under more intense currents, we tested the MHD conduction prototype shown in the diagram in Figure 3.12.

At the bottom is a link to a video of the test run using this prototype ‡. As can easily be seen, by setting a 5 A current through the galinstan under the application of a static magnetic field with an intensity between 0.18 and 0.1 T in the galinstan channel boundaries, we were able to induce quite a considerable flow. This leads us to conclude that the problem with the MHD induction prototype is partly that we are not able to induce currents of a sufficiently high magnitude to pump the galinstan. In the future, electromagnetic flow meters could be used to estimate the flow rate of these fluids. These measure the flow rate through the voltage induced in them due to the temporal variation caused by the movement of the fluid.

---

‡https://drive.google.com/drive/folders/1uiI-cnJzghCmQhU3Ey6WHAcXGwv5KZ6i?usp=sharing
Flow rate induced by the MHD conduction prototype

Chapter 5

Conclusions and future work

The work of this thesis was divided into 4 main parts: i) Fabrication of galinstan, the MCM alloy and the mixtures of galinstan and MCM particles; ii) Thermomagnetic convection prototype testing; iii) COMSOL simulations of an MHD induction pump; iv) Testing of two MHD pumping prototypes, inductive and conductive.

SEM-EDS analysis of the galinstan produced indicates an approximate elemental composition of 68 wt% Ga, 22 wt% In, 10 wt% Sn, which is the same as the expected composition of 68:22:10. DSC measurements showed two melting peaks starting at T=9.8 ℃, as well as two peaks during the cooling process at T=0.6 ℃ and T=-26 ℃. As discussed above, in the literature there is great variability in the DSC data for this alloy, nevertheless it should be noted that the melting and solidification points are close to those reported in literature.

Regarding the Gd-Si-Ge alloy, a LeBail refinement revealed a composition of around 75% Orthorhombic phase I and 25% Monoclinic phase. SEM images of the powder made it possible to study the distribution of particle sizes, obtaining an average size of 1.08 μm. Using SQUID measurements, it was possible to determine the T_c of our powder, obtaining 33.8 ℃ for the cooling protocol. It was also possible to quantify the magnetocaloric effect, obtaining a ΔS_M peak of 9 $Jkg^{-1}K^{-1}$ at around 36.9 ℃. The magnetic transition was also observed through DSC measurements.

Three mixtures were fabricated with nominal loadings of 2 wt%, 4 wt% and 6 wt%. Using SEM-EDS, it was possible to observe an irregular distribution of particles in the galinstan. It was found that they were dispersed in a non-uniform way with some clusters of particles. In order to quantify the true loading of particles dispersed in the galinstan,

SQUID measurements were used, but the study was inconclusive due to the great variability of the loadings determined for different samples. This is due to the non-uniformity of the fluid. However, it was immediately apparent that the calculated loadings are considerably lower (the maximum determined loading being of 0.35 wt% for a nominal loading of 6 wt%) than the target loadings, due to the loss of particles in the mortar when preparing the mixture as well as through successive pipetting processes which result in the loss of particles on the walls of the pipette. In summary, galinstan and a Gd-Si-Ge alloy have been successfully produced, we also produced a mixtures of these two components that can now be used in heat dissipator prototypes as well as in various other applications. Regarding future work, we can advance in many ways: i) Investigate the solubility of other MCMs in galinstan in order to maximize particle loadings; ii) Explore alternative processes for incorporating MCM particles into galinstan; iii) Carry out a more extensive statistical study in order to analyze the variability between loadings of samples of the same mixture; iv) Store the produced mixtures on containers filled with an acidic solution in order to reduce the particle losses within the eppendorfs.

On the second part, the mixtures were used in the thermomagnetic convection prototype. The thermal profiles obtained for a temperature gradient of 7 ºC with and without magnetic field showed no significant flow of the mixtures in the channel as there was no significant discrepancies between them. A future iteration of the prototype should pass by: i) Increasing the mixtures uniformity; ii) Increasing the effective loading of particles mixed in the galinstan, this may require the use of new alloys whose solubility in galinstan is higher; iii) Also the prototype can be tested with higher sets of temperature gradients.

In the third part an MHD induction pumping prototype was then simulated in COMSOL. Having obtained the magnetic field distribution along the geometry, and now making this field variable in time, we were able to determine the distribution of induced currents in the galinstan channel as well as the Lorentz force that arises through the coupling between the magnetic field and the currents. By solving the Navier-Stokes equation for the laminar regime, it was possible to study the velocity profile induced in the galinstan over time. We also analyzed the dependence of the equilibrium velocity reached by the galinstan (upwards of 33 cm/s) on the frequency of rotation of the permanent magnets, predicting a linear increase as documented in the literature for low magnetic field frequencies. A next step in this phase would be to include a COMSOL thermal study in the simulations in order to analyze the system's heat dissipation capabilities.

This prototype was later manufactured and tested with our galinstan. With the help of thermal profiles taken for a rotor frequency of 0 and 2.7 Hz, no significant galinstan flow could be observed, contrary to what was expected from the simulation. This was partly due to the fact that the high surface tension of the fluid was not included in the COMSOL model, thus presenting an extra barrier to the start of the fluid's movement. On the other hand, as observed in the thermal profiles, there is Joule heating due to the induced currents, so there is no perfect coupling of the magnetic field with the current as in the simulation. A future iteration will aim to increase the induced pumping force. This force depends on several factors, such as the magnitude of the magnetic field and the induced currents. These factors can be improved in various ways: i) The magnitude of the magnetic field can be increased by using a larger mass of magnets and reducing the distance from the magnet rotor to the galinstan channel; ii) The magnitude of the induced currents can be enhanced by increasing the magnetic field frequency, this can be achieved by using a greater number of permanent magnets in order to increase the periodicity of the magnetic field distribution; iii) Utilize coils thus allowing the magnetic field to switch much faster, at the cost of a lower magnetic field intensity.

Finally, we tested the MHD conduction prototype and observed a considerable flow of galinstan in our channel, which leads us to conclude that the magnitude of the currents we are inducing in the MHD induction prototype are not large enough to induce movement. In the future, electromagnetic flow meters could be used to estimate the flow rate of these fluids. These simply consist in coils that measure the flow rate through the voltage induced in them due to the temporal variation caused by the movement of the fluid.

This work thus serve as a starting point for further research on the subject, whether in fluid engineering, COMSOL simulations or the optimization of each of the three prototypes.

Bibliography

[1] Electrical4U, "Application of power electronics," Oct 2020. [Online]. Available: https://www.electrical4u.com/application-of-power-electronics/ [Cited on page 1.]

[2] K. Ma and J. Liu, "Liquid metal cooling in thermal management of computer chips," *Frontiers of Energy and Power Engineering in China*, vol. 1, no. 4, pp. 384–402, 2007. [Online]. Available: https://doi.org/10.1007/s11708-007-0057-3 [Cited on page 1.]

[3] E. Laloya, Lucía, H. Sarnago, and J. M. Burdío, "Heat management in power converters: From state of the art to future ultrahigh efficiency systems," *IEEE Transactions on Power Electronics*, vol. 31, no. 11, pp. 7896–7908, 2016. [Cited on page 1.]

[4] B. L. Rakshith, L. G. Asirvatham, A. A. Angeline, S. Manova, J. R. Bose, J. P. Selvin Raj, O. Mahian, and S. Wongwises, "Cooling of high heat flux miniaturized electronic devices using thermal ground plane: An overview," *Renewable and Sustainable Energy Reviews*, vol. 170, p. 112956, 2022. [Online]. Available: https://www.sciencedirect.com/science/article/pii/S1364032122008371 [Cited on pages xi and 1.]

[5] X.-H. Yang and J. Liu, "Chapter four - advances in liquid metal science and technology in chip cooling and thermal management," ser. Advances in Heat Transfer, E. M. Sparrow, J. P. Abraham, and J. M. Gorman, Eds. Elsevier, 2018, vol. 50, pp. 187–300. [Online]. Available: https://www.sciencedirect.com/science/article/pii/S0065271718300030 [Cited on page 2.]

[6] S. Sarkar, R. Gupta, T. Roy, R. Ganguly, and C. M. Megaridis, "Review of jet impingement cooling of electronic devices: Emerging role of surface engineering," *International Journal of Heat and Mass Transfer*, vol. 206, p. 123888,

2023. [Online]. Available: https://www.sciencedirect.com/science/article/pii/S0017931023000443 [Cited on page 2.]

[7] M. Hodes, R. Zhang, L. S. Lam, R. Wilcoxon, and N. Lower, "On the potential of galinstan-based minichannel and minigap cooling," *IEEE Transactions on Components, Packaging and Manufacturing Technology*, vol. 4, no. 1, pp. 46–56, 2014. [Cited on page 2.]

[8] C. O. Maidana and J. E. Nieminen, "First studies for the development of computational tools for the design of liquid metal electromagnetic pumps," *Nuclear Engineering and Technology*, vol. 49, no. 1, pp. 82–91, 2017. [Online]. Available: https://www.sciencedirect.com/science/article/pii/S1738573316301036 [Cited on page 2.]

[9] I. A. de Castro, A. F. Chrimes, A. Zavabeti, K. J. Berean, B. J. Carey, J. Zhuang, Y. Du, S. X. Dou, K. Suzuki, R. A. Shanks, R. Nixon-Luke, G. Bryant, K. Khoshmanesh, K. Kalantar-zadeh, and T. Daeneke, "A gallium-based magnetocaloric liquid metal ferrofluid," *Nano Lett.*, vol. 17, no. 12, pp. 7831–7838, Dec. 2017. [Online]. Available: https://doi.org/10.1021/acs.nanolett.7b04050 [Cited on pages 2, 6, and 36.]

[10] Y. Lu, H. Zhou, H. Mao, S. Tang, L. Sheng, H. Zhang, and J. Liu, "Liquid metal-based magnetorheological fluid with a large magnetocaloric effect." vol. 12, pp. 48 748– 48 755. [Cited on pages 2 and 6.]

[11] Y. Yerasimou, "Heat sinks based on liquid metal for power electronics cooling applications," Ph.D. dissertation, School of Engineering Newcastle University, 2020. [Cited on page 2.]

[12] L. S, S. K, M. S, and N. K., "Ga-based alloys in microelectronic interconnects: A review," *Materials (Basel). 2018 Aug 8;11(8):1384. doi:*, vol. 10., 2018. [Cited on page 3.]

[13] N. Yang, X. Sun, Y. Zhou, X. Yang, J. You, Z. Yu, J. Ge, F. Gong, Z. Xiao, Y. Jin, Z. Liu, and L. Cheng, "Liquid metal microspheres with an eddy-thermal effect for magnetic hyperthermia-enhanced cancer embolization-immunotherapy," *Science Bulletin*, 2023. [Online]. Available: https://www.sciencedirect.com/science/article/pii/S2095927323004607 [Cited on page 3.]

[14] S. S. Leonchuk, A. S. Falchevskaya, V. Nikolaev, and V. V. Vinogradov, "Nak alloy: underrated liquid metal," *J. Mater. Chem. A*, vol. 10, pp. 22 955–22 976, 2022. [Online]. Available: http://dx.doi.org/10.1039/D2TA06882F [Cited on page 3.]

[15] M. Williams, "The world's largest liquid-mirror telescope comes online," Jun 2022. [Online]. Available: https://www.universetoday.com/156246/the-worlds-largest-liquid-mirror-telescope-comes-online/ [Cited on page 3.]

[16] P. Q. Liu, X. Miao, and S. Datta, "Recent advances in liquid metal photonics: technologies and applications

invited

," *Opt. Mater. Express*, vol. 13, no. 3, pp. 699–727, Mar 2023. [Online]. Available: https://opg.optica.org/ome/abstract.cfm?URI=ome-13-3-699 [Cited on page 3.]

[17] G. Li, M. Zhang, S. Liu, M. Yuan, J. Wu, M. Yu, L. Teng, Z. Xu, J. Guo, G. Li, Z. Liu, and X. Ma, "Three-dimensional flexible electronics using solidified liquid metal with regulated plasticity," *Nature Electronics*, vol. 6, no. 2, pp. 154–163, 2023. [Online]. Available: https://doi.org/10.1038/s41928-022-00914-8 [Cited on page 3.]

[18] H. K. Patenaude and F. J. Freibert, "Oh, my darling clementine: A detailed history and data repository of the los alamos plutonium fast reactor," *Nuclear Technology*, vol. 209, no. 7, pp. 963–1007, 2023. [Online]. Available: https://doi.org/10.1080/00295450.2023.2176686 [Cited on page 3.]

[19] P. SL, K. EL, and S. S., *Mercury Toxicity*. In: StatPearls [Internet], 2023. [Cited on page 3.]

[20] G. J and M. N., *In-depth review of atmospheric mercury: sources, transformations, and potential sinks*. Energy and Emission Control Technologies, 2014. [Cited on page 3.]

[21] ""mercury"." [Online]. Available: https://environment.ec.europa.eu/topics/chemicals/mercury_en [Cited on page 3.]

[22] A. Abou-Sena, F. Arbeiter, and T. Böttcher, "Study of the wettability of fusion relevant steels by the sodium potassium eutectic alloy nak-78," *Nuclear Materials and Energy*, vol. 9, pp. 292–299, 2016. [Online]. Available: https://www.sciencedirect.com/science/article/pii/S2352179115300880 [Cited on page 4.]

[23] E. L. Smith, A. P. Abbott, and K. S. Ryder, "Deep eutectic solvents (dess) and their applications," vol. 114, no. 21, pp. 11 060–11 082. [Online]. Available: https://doi.org/10.1021/cr300162p [Cited on pages xi and 4.]

[24] H. S. B. Lee S. Mason and D. C. Hainley, "Sp- 100 power system conceptual design for lunar base applications." [Cited on page 4.]

[25] J. M. R. M. Mark Matney, Phillip Anz-Meador and T. Kennedy, "The nak population: a 2019 status," *https://ntrs.nasa.gov/citations/20190033494*, 2019. [Cited on page 4.]

[26] H. Butler, "Danamics lmx superleggera cooler review," May 2010. [Online]. Available: https://www.bit-tech.net/reviews/tech/cooling/danamics-lmx-superleggera-review/1/ [Cited on page 4.]

[27] N. O. of Response and U. G. Restoration. [Online]. Available: https://cameochemicals.noaa.gov/chemical/1525 [Cited on page 4.]

[28] Y. Lin, J. Genzer, and M. D. Dickey, "Attributes, fabrication, and applications of gallium-based liquid metal particles," *Advanced Science*, vol. 7, no. 12, p. 2000192, 2020. [Online]. Available: https://onlinelibrary.wiley.com/doi/abs/10.1002/advs.202000192 [Cited on page 4.]

[29] G. Bo, L. Ren, X. Xu, Y. Du, and S. Dou, "Recent progress on liquid metals and their applications," *Advances in Physics: X*, vol. 3, no. 1, p. 1446359, 2018. [Online]. Available: https://doi.org/10.1080/23746149.2018.1446359 [Cited on page 4.]

[30] Y. Plevachuk, V. Sklyarchuk, S. Eckert, G. Gerbeth, and R. Novakovic, "Thermophysical properties of the liquid ga-in-sn eutectic alloy," *J. Chem. Eng. Data*, vol. 59, no. 3, pp. 757–763, Mar. 2014. [Online]. Available: https://doi.org/10.1021/je400882q [Cited on page 4.]

[31] S. Schreiber, M. Minute, G. Tornese, R. Giorgi, M. Duranti, L. Ronfani, and E. Barbi, "Galinstan thermometer is more accurate than digital for the measurement of body temperature in children." *Pediatric emergency care*, vol. 29, pp. 197–9, Feb 2013. [Cited on page 5.]

[32] S. Porter, "All about ps5 liquid metal," Jul 2023. [Online]. Available: https://tronicsfix.com/blogs/news/all-about-ps5-liquid-metal [Cited on page 5.]

[33] P. Geddis, L. Wu, A. McDonald, S. Chen, and B. Clements, "Effect of static liquid galinstan on common metals and non-metals at temperatures up to 200 °c," *Canadian Journal of Chemistry*, vol. 98, no. 12, pp. 787–798, 2020. [Online]. Available: https://doi.org/10.1139/cjc-2020-0227 [Cited on page 5.]

[34] K. Y. Kwon, V. K. Truong, F. Krisnadi, S. Im, J. Ma, N. Mehrabian, T.-i. Kim, and M. D. Dickey, "Surface modification of gallium-based liquid metals: Mechanisms and applications in biomedical sensors and soft actuators," *Advanced Intelligent Systems*, vol. 3, no. 3, p. 2000159, 2021. [Online]. Available: https://onlinelibrary.wiley.com/doi/abs/10.1002/aisy.202000159 [Cited on page 5.]

[35] T. Daeneke, K. Khoshmanesh, N. Mahmood, I. A. de Castro, D. Esrafilzadeh, S. J. Barrow, M. D. Dickey, and K. Kalantar-zadeh, "Liquid metals: fundamentals and applications in chemistry," *Chem. Soc. Rev.*, vol. 47, pp. 4073–4111, 2018. [Online]. Available: http://dx.doi.org/10.1039/C7CS00043J [Cited on pages xi, 5, 18, 34, and 35.]

[36] S. Tang, T. He, H. Yu, Z. Ou, Z. Ren, M. Li, and W. Sheng, "A novel coating to avoid corrosion effect between eutectic gallium–indium alloy and heat sink metal for X-ray optics cooling," *Review of Scientific Instruments*, vol. 93, no. 12, p. 123102, 12 2022. [Online]. Available: https://doi.org/10.1063/5.0127785 [Cited on page 5.]

[37] M. R. Khan, C. B. Eaker, E. F. Bowden, and M. D. Dickey, "Giant and switchable surface activity of liquid metal via surface oxidation." *Proceedings of the National Academy of Sciences of the United States of America*, vol. 111, pp. 14 047–51, Sep 2014. [Cited on page 5.]

[38] V. Sivan, S.-Y. Tang, A. P. O'Mullane, P. Petersen, N. Eshtiaghi, K. Kalantar-zadeh, and A. Mitchell, "Liquid metal marbles," *Advanced Functional Materials*, vol. 23, no. 2, pp. 144–152, 2013. [Online]. Available: https://onlinelibrary.wiley.com/doi/abs/10.1002/adfm.201200837 [Cited on page 5.]

[39] M. D. Dickey, "Emerging applications of liquid metals featuring surface oxides," *ACS Appl. Mater. Interfaces*, vol. 6, no. 21, pp. 18 369–18 379, Nov. 2014. [Online]. Available: https://doi.org/10.1021/am5043017 [Cited on pages xi, 5, and 6.]

[40] J.-H. So and M. D. Dickey, "Inherently aligned microfluidic electrodes composed of liquid metal," *Lab Chip*, vol. 11, pp. 905–911, 2011. [Online]. Available: http://dx.doi.org/10.1039/C0LC00501K [Cited on page 5.]

[41] X. Wang, L. Li, X. Yang, H. Wang, J. Guo, Y. Wang, X. Chen, and L. Hu, "Electrically induced wire-forming 3d printing technology of gallium-based low melting point metals," *Advanced Materials Technologies*, vol. 6, no. 11, p. 2100228, 2021. [Online]. Available: https://onlinelibrary.wiley.com/doi/abs/10.1002/admt.202100228 [Cited on page 5.]

[42] X. He, M. Ni, J. Wu, S. Xuan, and X. Gong, "Hard-magnetic liquid metal droplets with excellent magnetic field dependent mobility and elasticity," *Journal of Materials Science Technology*, vol. 92, pp. 60–68, 2021. [Online]. Available: https://www.sciencedirect.com/science/article/pii/S1005030221003534 [Cited on page 6.]

[43] L. Hu, H. Wang, X. Wang, X. Liu, J. Guo, and J. Liu, "Magnetic liquid metals manipulated in the three-dimensional free space," vol. 11, no. 8, pp. 8685–8692. [Online]. Available: https://doi.org/10.1021/acsami.8b22699 [Cited on page 6.]

[44] E. Warburg, *Ann. Phys*, vol. 13, p. 141, 1881. [Cited on page 6.]

[45] K. A. Gschneidner, V. K. Pecharsky, and A. O. Tsokol, "Recent developments in magnetocaloric materials," *Reports on Progress in Physics*, vol. 68, no. 6, p. 1479, may 2005. [Online]. Available: https://dx.doi.org/10.1088/0034-4885/68/6/R04 [Cited on page 7.]

[46] V. K. Pecharsky and K. A. Gschneidner Jr, "Magnetocaloric effect and magnetic refrigeration," *Journal of Magnetism and Magnetic Materials*, vol. 200, no. 1, pp. 44–56, 1999. [Online]. Available: https://www.sciencedirect.com/science/article/pii/S0304885399003972 [Cited on pages xi and 7.]

[47] V. Franco, J. Blázquez, B. Ingale, and A. Conde, "The magnetocaloric effect and magnetic refrigeration near room temperature: Materials and models," *Annual Review of Materials Research*, vol. 42, no. 1, pp. 305–342, 2012. [Online]. Available: https://doi.org/10.1146/annurev-matsci-062910-100356 [Cited on pages xi and 8.]

[48] W. F. Giauque and D. P. MacDougall, "Attainment of temperatures below 1°
absolute by demagnetization of $gd_2(SO_4)_3 \cdot 8h_2o$," *Phys. Rev.*, vol. 43, pp. 768–768,
May 1933. [Online]. Available: https://link.aps.org/doi/10.1103/PhysRev.43.768
[Cited on page 8.]

[49] X. Tang, H. Sepehri-Amin, N. Terada, A. Martin-Cid, I. Kurniawan, S. Kobayashi,
Y. Kotani, H. Takeya, J. Lai, Y. Matsushita, T. Ohkubo, Y. Miura, T. Nakamura, and
K. Hono, "Magnetic refrigeration material operating at a full temperature range
required for hydrogen liquefaction," *Nature Communications*, vol. 13, no. 1, p. 1817,
2022. [Online]. Available: https://doi.org/10.1038/s41467-022-29340-2 [Cited on
page 8.]

[50] H. Ansarinasab, M. Fatimah, and Y. Khojasteh-Salkuyeh, "Conceptual design
of two novel hydrogen liquefaction processes using a multistage active
magnetic refrigeration system," *Applied Thermal Engineering*, vol. 230, p. 120771,
2023. [Online]. Available: https://www.sciencedirect.com/science/article/pii/
S1359431123008001 [Cited on page 8.]

[51] V. K. Pecharsky and K. A. Gschneidner, Jr., "Giant magnetocaloric effect in
$gd_5(si_2ge_2)$," *Phys. Rev. Lett.*, vol. 78, pp. 4494–4497, Jun 1997. [Online]. Avail-
able: https://link.aps.org/doi/10.1103/PhysRevLett.78.4494 [Cited on pages xi, 8,
and 10.]

[52] I. t. Have, "Reinventing the fridge: Why we invested in magnotherm," Apr
2023. [Online]. Available: https://medium.com/extantia-capital/reinventing-the-
fridge-why-we-invested-in-magnotherm-6efa0ba8b71b [Cited on page 8.]

[53] C. Ltd, Jul 2023. [Online]. Available: https://camfridge.com/ [Cited on page 8.]

[54] F. C. i Fernàndez, "Magnetocaloric effect in gd5(sixge1x)4 alloys," Ph.D. disserta-
tion, Universitat de Barcelona, 2003. [Cited on page 8.]

[55] M. Ghahremani, A. Aslani, M. Hosseinnia, L. H. Bennett, and E. Della Torre, "Direct
and indirect measurement of the magnetocaloric effect in bulk and nanostructured
Ni-Mn-In Heusler alloy," *AIP Advances*, vol. 8, no. 5, p. 056426, 01 2018. [Online].
Available: https://doi.org/10.1063/1.5007223 [Cited on page 9.]

[56] [Online]. Available: http://magnetocaloric.web.ua.pt/mce.html [Cited on page 9.]

[57] S. Ridha, D. Essebti, and E. K. Hlil, "Impact of annealing temperature on the physical properties of the lanthanum deficiency manganites," *Crystals*, vol. 7, no. 10, 2017. [Online]. Available: https://www.mdpi.com/2073-4352/7/10/301 [Cited on page 9.]

[58] C. Rodrigues, A. Pires, I. Gonçalves, D. Silva, J. OIiveira, A. Pereira, and J. Ventura, "Hybridizing triboelectric and thermomagnetic effects: A novel low-grade thermal energy harvesting technology," *Advanced Functional Materials*, vol. 32, no. 21, p. 2110288, 2022. [Online]. Available: https://onlinelibrary.wiley.com/doi/abs/10.1002/adfm.202110288 [Cited on page 10.]

[59] J. Y. Law, V. Franco, L. M. Moreno-Ramírez, A. Conde, D. Y. Karpenkov, I. Radulov, K. P. Skokov, and O. Gutfleisch, "A quantitative criterion for determining the order of magnetic phase transitions using the magnetocaloric effect," *Nature Communications*, vol. 9, no. 1, p. 2680, 2018. [Online]. Available: https://doi.org/10.1038/s41467-018-05111-w [Cited on page 10.]

[60] M. Almanza, A. Pasko, F. Mazaleyrat, and M. LoBue, "First- versus second-order magnetocaloric material for thermomagnetic energy conversion," *IEEE Transactions on Magnetics*, vol. 53, no. 11, pp. 1–6, 2017. [Cited on page 11.]

[61] Y. Mo and I. Szlufarska, "Single hot contacts," *Nature Materials*, vol. 12, no. 1, pp. 9–11, 2013. [Online]. Available: https://doi.org/10.1038/nmat3506 [Cited on pages xi and 11.]

[62] F. Guillou, G. Porcari, H. Yibole, N. van Dijk, and E. Brück, "Taming the first-order transition in giant magnetocaloric materials," *Advanced Materials*, vol. 26, no. 17, pp. 2671–2675, 2014. [Online]. Available: https://onlinelibrary.wiley.com/doi/abs/10.1002/adma.201304788 [Cited on page 11.]

[63] Belo, J. H., Amaral, J. S., and Ventura, J. O., "Near room-temperature thermomagnetic energy harvesting," *Europhysics News*, vol. 54, no. 3, pp. 20–23, 2023. [Online]. Available: https://doi.org/10.1051/epn/2023302 [Cited on page 11.]

[64] N. Tesla, *Thermo-Magnetic Motor*. (United States Patent Office, Patent No 396,121), 1889. [Online]. Available: https://patents.google.com/patent/US396121A/en#citedBy [Cited on pages xi and 12.]

[65] R. A. Kishore and S. Priya, "A review on design and performance of thermomagnetic devices," *Renewable and Sustainable Energy Reviews*, vol. 81, pp. 33–44, 2018. [Online]. Available: https://www.sciencedirect.com/science/article/pii/S1364032117311036 [Cited on page 12.]

[66] D. J. Griffiths, *Introduction to Electrodynamics*, 4th ed. Cambridge University Press, 2017. [Cited on page 12.]

[67] M. Khairul, E. Doroodchi, R. Azizian, and B. Moghtaderi, "Advanced applications of tunable ferrofluids in energy systems and energy harvesters: A critical review," *Energy Conversion and Management*, vol. 149, pp. 660–674, 2017. [Online]. Available: https://www.sciencedirect.com/science/article/pii/S0196890417306994 [Cited on page 12.]

[68] O. Oehlsen, S. I. Cervantes-Ramírez, P. Cervantes-Avilés, and I. A. Medina-Velo, "Approaches on ferrofluid synthesis and applications: Current status and future perspectives," *ACS Omega*, vol. 7, no. 4, pp. 3134–3150, Feb. 2022. [Online]. Available: https://doi.org/10.1021/acsomega.1c05631 [Cited on page 12.]

[69] V. Chaudhary, Z. Wang, A. Ray, I. Sridhar, and R. V. Ramanujan, "Self pumping magnetic cooling," *Journal of Physics D: Applied Physics*, vol. 50, no. 3, p. 03LT03, dec 2016. [Online]. Available: https://dx.doi.org/10.1088/1361-6463/aa4f92 [Cited on pages xii and 13.]

[70] F. G. L. F. Furriel, "Magnetocaloric ferrofluids," Ph.D. dissertation, Faculty of Science of the Porto University, 2021-11-24. [Cited on pages 14, 36, 40, and 46.]

[71] A. Tassone, "Study on liquid metal magnetohydrodynamic flows and numerical application to a water-cooled blanket for fusion reactors," Ph.D. dissertation, Sapienza Università di Roma, 2019. [Cited on page 14.]

[72] H. Ingals, "Darpa launches program in quest for "red october" silent submarine drive," Jun 2023. [Online]. Available: https://newatlas.com/military/darpa-launches-program-in-quest-for-red-october-silent-submarine-drive/ [Cited on page 14.]

[73] M. Majid, M. A.-H. M. Apandi, M. Sabri, and K. Shahril, "Fundamental studies on development of mhd (magnetohydrodynamic) generator implement on wave

energy harvesting," *IOP Conference Series: Materials Science and Engineering*, vol. 114, no. 1, p. 012145, feb 2016. [Online]. Available: https://dx.doi.org/10.1088/1757-899X/114/1/012145 [Cited on page 14.]

[74] L. Blake, "Electro-magnetic pumps for liquid metals," *Journal of Nuclear Energy. Part B. Reactor Technology*, vol. 1, no. 2, pp. 65–IN1, 1959. [Online]. Available: https://www.sciencedirect.com/science/article/pii/S0368327315300018 [Cited on page 14.]

[75] B. K. Nashine, S. K. Dash, K. Gurumurthy, M. Rajan, and G. Vaidyanathan, *Design and Testing of DC Conduction Pump for Sodium Cooled Fast Reactor*. United States: American Society of Mechanical Engineers - ASME, 2006. [Online]. Available: http://inis.iaea.org/search/search.aspx?orig_q=RN:39019554 [Cited on page 14.]

[76] A. V. Lemoff and A. P. Lee, "An ac magnetohydrodynamic micropump," *Sensors and Actuators B: Chemical*, vol. 63, no. 3, pp. 178–185, 2000. [Online]. Available: https://www.sciencedirect.com/science/article/pii/S0925400500003555 [Cited on page 15.]

[77] S. Lim and B. Choi, "A study on the mhd (magnetohydrodynamic) micropump with side-walled electrodes," *Journal of Mechanical Science and Technology*, vol. 23, no. 3, pp. 739–749, 2009. [Online]. Available: https://doi.org/10.1007/s12206-008-1107-0 [Cited on pages xii and 15.]

[78] L. Wang, Y. Hou, L. Shi, Y. Wu, W. Tian, D. Song, S. Qiu, and G. Su, "Experimental study and optimized design on electromagnetic pump for liquid sodium," *Annals of Nuclear Energy*, vol. 124, pp. 426–440, 2019. [Online]. Available: https://www.sciencedirect.com/science/article/pii/S0306454918305413 [Cited on page 15.]

[79] C. Liu and Z. He, "High heat flux thermal management through liquid metal driven with electromagnetic induction pump," *Frontiers in Energy*, vol. 16, no. 3, pp. 460–470, 2022. [Online]. Available: https://doi.org/10.1007/s11708-022-0825-9 [Cited on pages xii and 15.]

[80] I. Bucenieks, "High pressure and high flowrate induction pumps with permanent magnets," *Magnetohydrodynamics*, vol. 39, pp. 411–418, 11 2003. [Cited on page 16.]

[81] I. A. de Castro, A. F. Chrimes, A. Zavabeti, K. J. Berean, B. J. Carey, J. Zhuang, Y. Du, S. X. Dou, K. Suzuki, R. A. Shanks, R. Nixon-Luke, G. Bryant, K. Khoshmanesh, K. Kalantar-zadeh, and T. Daeneke, "Supporting information: A gallium-based magnetocaloric liquid metal ferrofluid," *Nano Lett.*, vol. 17, no. 12, pp. 7831–7838, Dec. 2017. [Online]. Available: https://doi.org/10.1021/acs.nanolett.7b04050 [Cited on page 17.]

[82] T. S. C. . F. Scientific. [Online]. Available: https://www.fishersci.co.uk/shop/products/gallium-ingot-99-99-metals-basis-thermo-scientific/11391238 [Cited on page 17.]

[83] T. Scientific. [Online]. Available: https://www.fishersci.com/shop/products/indium-ingot-button-31mm-1-2-in-dia-x-5-3mm-0-21-in-thick-99-99-metals-basis-thermo-scientific/AA45111KF [Cited on page 17.]

[84] F. Scientific. [Online]. Available: https://www.fishersci.com/shop/products/tin-shot-3mm-0-1in-99-99-metals-basis-thermo-scientific/AA3664122 [Cited on page 17.]

[85] V. L. Stout and M. D. Gibbons, "Gettering of Gas by Titanium," *Journal of Applied Physics*, vol. 26, no. 12, pp. 1488–1492, Dec. 1955. [Cited on page 19.]

[86] D. Barsuk, "Metallurgical design of new nanoporous structures," Ph.D. dissertation, 10 2017. [Cited on pages xii and 19.]

[87] J. Jordan, "What is x-ray diffraction?" Oct 2016. [Online]. Available: https://www.jeremyjordan.me/what-is-x-ray-diffraction/ [Cited on pages xii and 21.]

[88] J. M. Thomas, "The birth of x-ray crystallography," vol. 491, no. 7423, pp. 186–187. [Online]. Available: https://doi.org/10.1038/491186a [Cited on page 21.]

[89] M. Tilli and A. Haapalinna, "Chapter 1 - properties of silicon," in *Handbook of Silicon Based MEMS Materials and Technologies (Second Edition)*, second edition ed., ser. Micro and Nano Technologies, M. Tilli, T. Motooka, V.-M. Airaksinen, S. Franssila, M. Paulasto-Kröckel, and V. Lindroos, Eds. Boston: William Andrew Publishing, 2015, pp. 3–17. [Online]. Available: https://www.sciencedirect.com/science/article/pii/B9780323299657000014 [Cited on page 22.]

[90] Q. Design, *Magnetic property measurement system - mpms 3 users manual*, 2016. [Cited on pages xii, 22, and 23.]

[91] R. L. Fagaly, "Superconducting quantum interference device instruments and applications," *Review of Scientific Instruments*, vol. 77, no. 10, p. 101101, 10 2006. [Online]. Available: https://doi.org/10.1063/1.2354545 [Cited on page 22.]

[92] *Light Microscopy*. John Wiley Sons, Ltd, 2013, ch. 1, pp. 1–45. [Online]. Available: https://onlinelibrary.wiley.com/doi/abs/10.1002/9783527670772.ch1 [Cited on page 24.]

[93] A. Ul-Hamid, *Components of the SEM*. Cham: Springer International Publishing, 2018, pp. 15–76. [Online]. Available: https://doi.org/10.1007/978-3-319-98482-7_2 [Cited on page 24.]

[94] S. E. M. . C. M. R. Facility. [Online]. Available: https://cmrf.research.uiowa.edu/scanning-electron-microscopy [Cited on page 24.]

[95] "Different types of sem imaging – bse and secondary electron imaging," Jan 2020. [Online]. Available: https://www.azom.com/article.aspx?ArticleID=14309 [Cited on pages xii and 24.]

[96] L. Reimer, "Scanning electron microscopy: Physics of image formation and microanalysis, second edition," *Measurement Science and Technology*, vol. 11, p. 1826, 11 2000. [Cited on page 25.]

[97] P. Gill, T. T. Moghadam, and B. Ranjbar, "Differential scanning calorimetry techniques: applications in biology and nanoscience." vol. 21, pp. 167–93. [Cited on page 25.]

[98] S. Lindersson, *Reactivity of Galinstan with Specific Transition Metal Carbides (Dissertation)*, 2014. [Cited on page 25.]

[99] Oct 2022. [Online]. Available: https://www.linseis.com/en/applications/polymers/chip-dsc-10-polymers-pet/ [Cited on pages xii and 26.]

[100] Q. Yu, Q. Zhang, J. Zong, S. Liu, X. Wang, X. Wang, H. Zheng, Q. Cao, D. Zhang, and J. Jiang, "Identifying surface structural changes in a newly-developed ga-based alloy with melting temperature below 10°c," *Applied Surface Science*, vol. 492,

pp. 143–149, 2019. [Online]. Available: https://www.sciencedirect.com/science/article/pii/S0169433219319191 [Cited on page 34.]

[101] B. Wang, J. Maslik, O. Hellman, A. Gumiero, and K. Hjort, "Supercooled liquid ga stretchable electronics," *Advanced Functional Materials*, vol. 33, no. 29, p. 2300036, 2023. [Online]. Available: https://onlinelibrary.wiley.com/doi/abs/10.1002/adfm.202300036 [Cited on page 34.]

[102] J. Ma and P. Zhang, "Supercooling suppression of phase change liquid metal–polydimethylsiloxane soft composites," *Mater. Adv.*, vol. 2, pp. 7437–7444, 2021. [Online]. Available: http://dx.doi.org/10.1039/D1MA00601K [Cited on page 34.]

[103] T. Cole and S.-Y. Tang, "Liquid metals as soft electromechanical actuators," *Mater. Adv.*, vol. 3, pp. 173–185, 2022. [Online]. Available: http://dx.doi.org/10.1039/D1MA00885D [Cited on page 35.]

[104] J. Mingjiang, Q. Li, R. Ying, X. Lu, X. Jin, and X. Ding, "Internal friction of phase transformations observed around room temperature in ga-in-sn eutectic alloys," *Archives of Metallurgy and Materials*, vol. 60, 09 2015. [Cited on pages 35 and 36.]

[105] S. Handschuh-Wang, T. Gan, M. Rauf, W. Yang, F. J. Stadler, and X. Zhou, "The subtle difference between galinstan (r) and eutectic gainsn," *Materialia*, vol. 26, p. 101642, 2022. [Online]. Available: https://www.sciencedirect.com/science/article/pii/S2589152922003234 [Cited on page 35.]

[106] A. Koh, W. Hwang, P. Y. Zavalij, S. Chun, G. Slipher, and R. Mrozek, "Solidification and melting phase change behavior of eutectic gallium-indium-tin," *Materialia*, vol. 8, p. 100512, 2019. [Online]. Available: https://www.sciencedirect.com/science/article/pii/S2589152919303084 [Cited on page 36.]

[107] S. Knappe, "Influences of heating and cooling rates on the dsc measurement result." [Online]. Available: https://analyzing-testing.netzsch.com/en/training-know-how/tips-tricks/dsc/influences-of-heating-and-cooling-rates-on-the-dsc-measurement-result [Cited on page 36.]

[108] S. Singh, N. Liu, Y. Zhang, A. Nozariasbmarz, S. K. Karan, L. Raman, G. K. Goyal, S. Sharma, W. Li, S. Priya, and B. Poudel, "High-performance thermomagnetic

gd-si-ge alloys," *ACS Appl. Mater. Interfaces*, vol. 15, no. 29, pp. 35 140–35 148, Jul. 2023. [Online]. Available: https://doi.org/10.1021/acsami.3c03158 [Cited on pages 37 and 39.]

[109] V. M. Andrade, N. B. Barroca, A. L. Pires, J. H. Belo, A. M. Pereira, K. R. Pirota, and J. P. Araújo, "Freestanding and flexible composites of magnetocaloric gd5(si,ge)4 microparticles embedded in thermoplastic poly(methyl methacrylate) matrix," *Materials Design*, vol. 186, p. 108354, 2020. [Online]. Available: https://www.sciencedirect.com/science/article/pii/S0264127519307920 [Cited on page 38.]

[110] X. Zhong, X. Feng, J. Huang, Y. Huang, Z. Liu, and R. Ramanujan, "Influence of particle size on the mechanical properties and magnetocaloric effect of la0.8ce0.2(fe0.95co0.05)11.8si1.2/sn composites," *Journal of Magnetism and Magnetic Materials*, vol. 463, pp. 23–27, 2018. [Online]. Available: https://www.sciencedirect.com/science/article/pii/S0304885318310114 [Cited on page 40.]

[111] E. Villa, C. Tomasi, A. Nespoli, F. Passaretti, G. Lamura, and F. Canepa, "Investigation of microstructural influence on entropy change in magnetocaloric polycrystalline samples of nimngacu ferromagnetic shape memory alloy," *Journal of Materials Research and Technology*, vol. 9, no. 2, pp. 2259–2266, 2020. [Online]. Available: https://www.sciencedirect.com/science/article/pii/S2238785419315662 [Cited on page 40.]

[112] O. Koplak, S. Kashin, and R. Morgunov, "Strain engineering of magnetocaloric effect in w/gd/w/mgo structures," *Journal of Magnetism and Magnetic Materials*, vol. 564, p. 170164, 2022. [Online]. Available: https://www.sciencedirect.com/science/article/pii/S0304885322010496 [Cited on page 40.]

[113] R. T. Smith, F. P. M. Jjunju, I. S. Young, S. Taylor, and S. Maher, "A physical model for low-frequency electromagnetic induction in the near field based on direct interaction between transmitter and receiver electrons." *Proceedings. Mathematical, physical, and engineering sciences*, vol. 472, p. 20160338, Jul 2016. [Cited on page 52.]